CYCLIC FATIGUE BEHAVIOR OF FRICTION STIR WELDED AZ-SERIES MAGNESIUM ALLOYS

Cyclic Fatigue Behavior of Friction Stir Welded AZ-Series Magnesium Alloys

by

© Fadi George Basmaji, B.Eng

A thesis
Submitted to the School of Graduate Studies
in Partial Fulfilment of the Requirements for
the Degree of
Master of Applied Science

Department of Materials Science and Engineering
McMaster University

September 2016

Hamilton Ontario

Abstract

Fully reversed stress controlled cyclic fatigue testing in ambient air was conducted on friction stir welded magnesium AZ31 and AZ61 to magnesium AZ80 specimens to study the fatigue behavior and properties of the weld and to grasp an understanding of the relationship between the material substructure and fatigue life. The resulting stress amplitude vs. cycles to failure (S-N) curves show an increase in fatigue life with a decrease in stress amplitude. For the AZ80/AZ31 weld, a sharp bend in the fatigue data was observed with an endurance limit of 70 MPa. A sharp bend was also observed in the AZ80/AZ61 weld which had an endurance limit of 90 MPa. Almost all the specimens fractured at the interface between the heat-affected zone of the weld and the AZ80 base material for both dissimilar welds. SEM fracture surface observations from the AZ80/AZ31 weld show crack initiation occurring from the surface and crack propagation through the material for the high and moderate stress amplitudes. The fracture surfaces were neither true brittle nor true ductile, instead, they were a combination of the both with evidence of secondary angled cracking. The fracture surfaces also exhibited macroscopic and microscopic features unique to fatigue failure, which includes fatigue striations and beach marks. Analysis of the material dislocation substructure was conducted using TEM microscopy for the AZ80/AZ31 specimens tested at a high stress, moderate stress, and the endurance limit stress. A difference in the dislocation substructures and densities is observed from the different specimens which can be related to the stress amplitude applied. X-ray diffraction was also conducted on specimens tested at a high stress, moderate stress, and the endurance limit stress, as well as a specimen that was undeformed. The pole figures show a strong initial basal texture for the undeformed specimen that becomes rotated off the tensile axis as the specimens are subjected to increasing fatigue damage. The pole figures for the moderate stress and the endurance limit stress show a basal texture rotation of approximately 85°.

Acknowledgements

First and foremost, I would like to express my deepest and heartfelt gratitude towards my supervisor, Dr. Marek Niewczas. His constant encouragement, patience, generosity and guidance throughout the course of my work was more than I could have asked for. It was a pleasure working with him, and I look forward to future opportunities to work with him again.

I would like to thank Dr. Anna Kula, a post-doctoral fellow in Dr. Niewczas′ group. Without her help and guidance during sample preparation and TEM sessions, this research work would not have ran so smoothly. Also, an extended thank you is sent to Dr. Fumiaki Hiura for his help and guidance throughout my research work.

I would also like to thank Victoria Jarvis and Dr. Jim Britten at McMaster University for their friendliness and guidance with X-Ray analysis. Their support and guidance, as well as valuable discussion, were necessary for this work. I am grateful for my colleagues in the AUTO21 research group, namely Dr. Brad Diak and Jessica Hiscocks from Queen′s University for their guidance, patience, and productive discussions. An extended thank you to Yuri Savguira at the University of Toronto for his help in sample preparation and discussions throughout my work.

Finally, I would like to thank my family and friends that constantly supported me through the rough and smooth times during all my years of university. Your motivation and encouragement throughout the years helped keep me focused on the goal at hand and to see the bigger picture. I would also like to thank, again, all the people mentioned or not mentioned here, and I would like to dedicate this thesis to all of them.

Dedicated to my parents.

They gave up everything, so I can have everything.

”For I know the plans I have for you,” declares the Lord, ”plans to prosper you and not to harm you, plans to give you hope and a future.”

- Jeremiah 29:11

List of Abbreviations

ASTM	**A**merican **S**ociety for **T**esting and **M**aterials
CRSS	**C**ritical **R**esolved **S**hear **S**tress
EBSD	**E**lectron **B**ack **S**catter **D**iffraction
HCP	**H**exagonal **C**lose **P**acked
SEM	**S**canning **E**lectron **M**icroscopy
TEM	**T**ransmission **E**lectron **M**icroscopy
UTS	**U**ltimate **T**ensile **S**tress
XRD	**X** - **R**ay **D**iffraction
S-N	**S**tress vs. **N**umber of Cycles
LCF	**L**ow **C**ycle **F**atigue
HCF	**H**igh **C**ycle **F**atigue
VHCF	**V**ery **H**igh **C**ycle **F**atigue
Nf	**N**umber of Cycles until **F**ailure
FSW	**F**riction **S**tir **W**eld
TMAZ	**T**hermo **M**echanically **A**ffected **Z**one
SZ	**S**tir **Z**one
HAZ	**H**eat **A**ffected **Z**one
NZ	**N**ugget **Z**one
WNZ	**W**eld **N**ugget **Z**one

List of Symbols

T	Temperature
b	Burgers Vector
σ_m	Stress
σ_a	Stress Amplitude
σ_m	Mean Stress
σ_y	Yield Stress
$\triangle\sigma$	Stress Range
ε	Strain
ρ_d	Dislocation Density
K	Kelvin
$^{\circ}C$	Degree Celsius
J	Joules
N	Newtons
kN	Kilonewton
m	Metre
cm	Centimetre
mm	Millimetre
μm	Micrometre
nm	Nanometre
at.%	Atomic Percent
wt.%	Weight Percent
R	Stress Ratio
f	Frequency

Contents

List of Tables

List of Figures

Chapter 1

Introduction

1.1 Background Information and Motivation

Magnesium and magnesium alloys have become increasingly more popular over the past decade for structural applications, especially in the aerospace and automotive industry. With recent fuel regulations set for the future, the automotive industry is challenged to produce lighter and more fuel efficient vehicles, while keeping passenger safety and comfort paramount. High strength steels, aluminum, and polymers are currently being used to reduce vehicle weight significantly, but further reductions can be made with the use of magnesium and its alloys. The combination of magnesium′s low density and good mechanical strength, contributes to its high strength-to-weight ratio. It is about 33% lighter than aluminum and about 80% lighter than iron when alloyed; magnesium has the potential to have the highest strength-to-weight ratio of all the structural metals available. Current vehicles are made of a combination of different materials, thus to incorporate magnesium alloys in a vehicle the joining process must be investigated.

A promising alloy for the aerospace and automotive industry has been in the past and is still currently a Mg-Al based alloy, especially the aluminum-zinc (AZ) and aluminum-manganese (AM) alloy series. However, the broad use of magnesium is limited due to its hexagonal close-packed (HCP) crystal structure. This crystal structure has a limited number of slip systems to accommodate deformation, resulting in limited ductility, especially at room temperature. However, most automotive applications require good ductility for many components, especially energy absorption in the case of an accident. The AZ31 magnesium alloy has been the most widely used magnesium alloy for commercial application, however, for some applications its strength does not meet the certain requirements. While the AZ80 magnesium alloy, with a higher aluminum content, has a higher strength in comparison to the AZ31 alloy but has a poor deformation ability. Thus, joining of AZ31 and AZ80 can further enlarge the application of magnesium alloys in the industry, by combining both the strength of AZ80 and the better ductility of AZ31. However, in general, the joining process often introduces a weaker element as it alters the microstructure and thus the properties of the materials.

1.2 Problem Statement and Scope of Thesis

A large number of structural and automotive components are subjected to cyclic loading throughout their service life, so an understanding of the material′s behaviour under these conditions is essential. The failure of materials under these cyclic conditions is referred to as fatigue. Fatigue failure accounts for approximately 90% of all mechanical service failures of components. This method of failure occurs at low stresses, often below the ultimate tensile strength of the material, that are much lower than the stress required to cause failure for a single application of stress [8]. Fatigue failure occurs suddenly and often without warning, potentially resulting in catastrophic consequences. It is imperative to study and understand the fatigue behavior of materials, especially in automotive applications, as an unexpected failure will result in the safety of the occupants of the vehicle and others around them to be compromised.

The fatigue behaviour of AZ31, AZ61 and AZ80 have been studied, however, the behaviour of the friction stir welds of these magnesium alloys has not been thoroughly investigated. As the mechanical behaviour under cyclic loading is directly related to safety issues, this is an important issue that must be addressed. Friction stir welding is a solid-state welding technique founded in 1991 by The Welding Institute [3]. It is a relatively new welding technique that offers promising final products that are suitable for automotive and aerospace applications. As a result of its solid-state nature, the properties of the welds are similar to the properties of the parent materials.

This project is carried out with the support of the AUTO21 Network of Centres of Excellence, it incorporates many universities across Canada, including Queen's University, University of Toronto, Waterloo University, University of Alberta, and McMaster University. The global vision of the project is to ultimately improve the fuel efficiency of a vehicle by reducing its weight. More specifically, it is focused on the development of an optimized low weight spare wheel, composed of AZ80 alloy for the hoop and the AZ31 or AZ61 alloys for the spokes. These materials will be friction stir welded together. The reasoning for this is to start with something that is used for a short period, to see if it is a viable option before moving to large-scale applications. The purpose of the present study is to evaluate the cyclic deformation behaviour in compressive and tensile loading-unloading conditions, and axial load-controlled fatigue behaviour of friction stir welded AZ31, AZ61, and AZ80 magnesium alloys. As well as, understanding the correlation between the fatigue behavior and identify the mechanisms underlying to the saturation stress and fatigue life in the welded magnesium alloys.

1.3 Thesis Organization

This thesis is comprised of six chapters, which are organized as follows: the first chapter provides a short introduction to the topic and states the motivation and objectives of the present work. In chapter two, background information about magnesium and its alloys, friction stir welding, and a general outline of fatigue is discussed. The experimental procedure of the stress-controlled fatigue tests, scanning electron microscopy, transmission electron microscopy, and texture measurements is described in chapter three. While chapter four summarizes the results and they are further discussed in chapter five. Finally, the findings of the present work are summarized in chapter six.

Chapter 2

Literature Review

2.1 Magnesium and Magnesium Alloys

Magnesium is one of the lightest structural metal available. Due to its light weight and mechanical properties, it offers a high strength-to-weight ratio, which makes it an attractive material for the aerospace and automotive industry [9]. Comparing stiffness to mass density ratios, magnesium alloys offer a significant advantage over steel and aluminum alloys. There is also a relatively high abundance of magnesium metal, as it comprises part of the earth′s crust and ocean waters [10].

With the increasing concerns of greenhouse gas emissions (GHGs), it has become an increasingly more important topic discussed by world leaders. The automotive industry, in particular, has been researching new ways to reduce the curb weight of a vehicle. In the past, there has been a shift in the materials used to tackle this problem; from the use of iron to high-strength steels, as well as aluminum and polymers. However, with magnesium′s low density and good mechanical properties, it is a promising material to include in vehicles to reduce the curb weight of the vehicle. The weight reduction can be translated to fuel savings and limiting the environmental impact of the vehicle by reducing the carbon dioxide, CO_2, emissions produced during the vehicle′s service life.

The structural applications of magnesium and its alloys inevitably involves welding and joining. Welding causes a weakening of the material′s properties due to microstructural changes produced and welding defects generated. Thus, the understanding and research of the microstructure evaluation, tensile properties, and fatigue behavior, as well as the optimization of the welding process is crucial in moving forward and using magnesium for structural applications.

2.1.1 Magnesium Alloys and Nomenclature

Pure magnesium is rarely used in the automotive and aerospace industry due to its volatility at high temperatures and its susceptibility to corrosion in wet environments. For structural applications, magnesium is more commonly alloyed with other elements to provide improved properties. Many alloying elements can provide beneficial properties in diverse applications, while others are used for more specific tasks. Magnesium has a hexagonally-packed structure with a c/a ratio of 1.624 and an atomic diameter of 0.320 nm which allows for a wide range of solutes to be solid soluble [11]. Common alloying elements with magnesium include aluminum, copper, manganese, rare-earth metals, yttrium, and zinc. The addition of each of these metals to the magnesium alloys provides varying effects. For example, the addition of aluminum as an alloying element in magnesium improves the strength and hardness, and it widens the freezing range which makes the alloy easier to cast [11]. Aluminum consists of $2-9$ $wt\%$ in most magnesium alloys, where the alloy can become heat treatable when the weight percent of aluminum is $> 6\%$. However, at increased amounts of aluminum, the ductility of the alloy decreases, but this does not deter the fact that aluminum is the most widely used alloying element with magnesium. Manganese is used as an alloying element to improve the corrosive resistance of magnesium alloys by removing iron present and forming relatively harmless intermetallic compounds. The presence of iron in magnesium greatly reduces the alloy′s corrosion resistance [11]. Zinc is another favorable alloying element, alongside aluminum, because it improves the room-temperature strength of the alloy. It also helps to reduce the impact of the presence of iron and other heavy metallic compounds that reduce the corrosion resistance of the alloy [11].

The standard system for naming magnesium alloys was accepted by the American Society for Testing and Materials (ASTM), more specifically it is outlined in the $B951-11$ standard. The first two letters designated for the alloy represent the major alloying elements added. For example in the magnesium alloy referred to as AZ31, the first letter ”A” represents aluminum as the largest alloy element. The number ”3” also refers to aluminum having a weight percent of $2.6-3.4$ %. The second letter, ”Z”, represents zinc as the second largest alloying element and the number ”1” implies that the alloy contains $0.6-1.4$ % of zinc. Table 2.1 shows the common letters used in alloy designation for magnesium [1].

Table 2.1: Magnesium alloying elements designation, according to the ASTM [1].

A - Aluminum	N - Nickel
B - Bismuth	P - Lead
C - Copper	R - Chromium
D - Cadmium	S - Silicon
E - Rare Earths	T - Tin
H - Thorium	W - Yttrium
K - Zirconium	Y - Antimony
M - Manganese	Z - Zinc

2.2 Deformation Mechanisms of Magnesium

2.2.1 Slip and Twinning

As it was previously mentioned, magnesium has a hexagonal closed-pack (HCP) structure. This crystal packing results in a lower symmetry in the system, which also entails that there are a limited number of slip systems. According to the von Mises$'$ condition; for a system to undergo a general plastic shape change, five independent slip systems must be able to operate [12]. The possible slips systems in HCP crystals are shown in Fig. 2.1 and summarized in Table 2.2. The four common slip systems for magnesium are basal $< a >$ slip $\{0002\}$, prismatic $< a >$ slip $\{10\bar{1}0\}$, 1^{st} order pyramidal $< c+a >$ slip $\{10\bar{1}1\}$, and 2^{nd} order pyramidal $< c+a >$ slip $\{11\bar{2}2\}$.

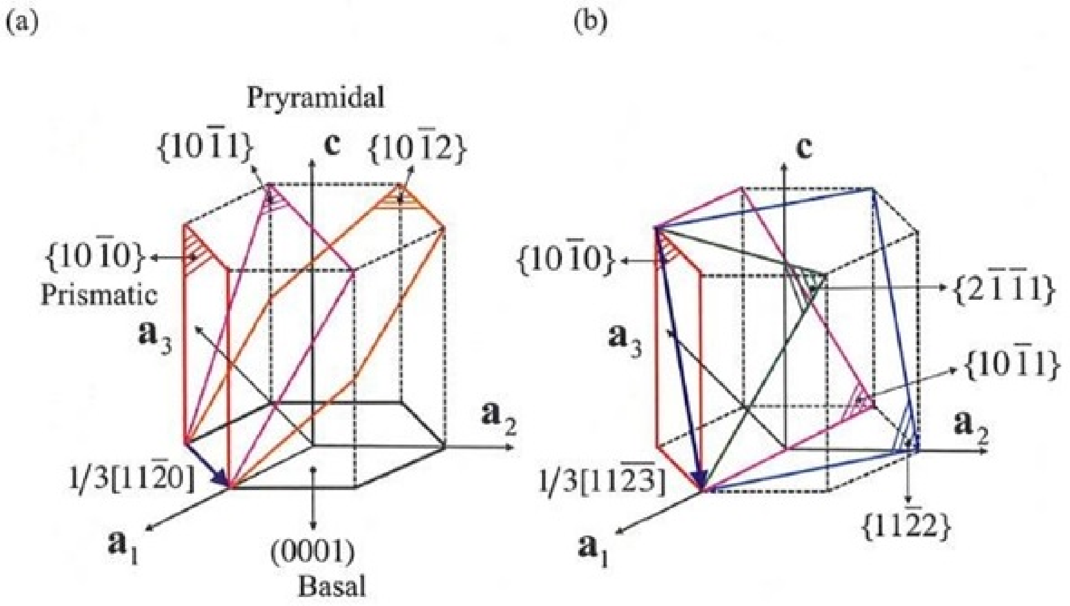

Figure 2.1: Slip systems in HCP crystals, a.) Basal, Prismatic, and Pyramidal slip systems with $< a >$ Burgers vector and, b.) four possible Pyramidal with $< c+a >$ Burgers vector [2].

Table 2.2: Independent modes of deformation in HCP crystals [2].

Direction	Plane	Crystallographic Elements {hkil}$< uvtw >$	Number of Independent Modes
$< a >$	Basal	{0001}$<$ 1120 $>$	2
	Prismatic	{10$\bar{1}$0} $<$ 1120 $>$	2
	Pyramidal	{1$\bar{1}$0l} $<$ 1120 $>$	4
$< c >$		{hki0} [0001]	
$< c+a >$	Pyramidal	{hkil}$<$ 1123 $>$	5
Twinning		$K_1 < \eta_1 >$	0 - 5

At room temperature, the deformation of magnesium and its alloys occurs by crystallographic slip and twinning. Whether slip or twinning will be the dominant mechanism depends on which of these two deformation modes is characterized by the lowest critical resolved shear stress (CRSS). The critical resolved shear stress is the component of shear stress that is resolved in the direction of slip, necessary to initiate slip in the material. The temperature dependence of the CRSS for the common slip systems is shown in Fig. 2.2.

From this figure, it is evident that basal slip is the easiest slip system active at room temperature because it has the lowest CRSS value, making it a prevailing deformation mechanism for magnesium. The CRSS of other slip systems, namely prismatic and pyramidal, is almost a hundred-fold larger than basal slip. However, at higher temperatures non-basal slip becomes easier to activate. From Table 2.2 it is apparent that basal slip has only two independent slip systems, which gives rise to the poor ductility and formability of polycrystalline magnesium and magnesium alloys. In fact, if the two most common slips, basal and prismatic, are activated simultaneously, they only offer four independent slip systems between them. When a slip system with a $< c+a >$ Burgers vector is operative, this

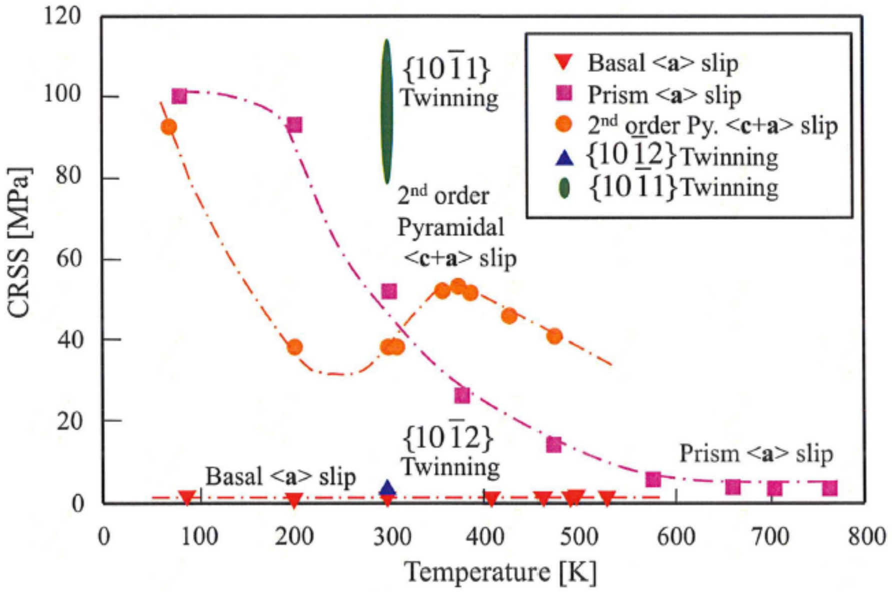

Figure 2.2: CRSS for the common slip systems in magnesium, courtesy of Fumiaki Hiura [4].

alone provides the necessary five independent modes to satisfy von Mises′ criteria. Due to the limited number of slip systems in magnesium, twinning plays an important role in the facilitation of deformation. The two common types of twins documented in magnesium and its alloys are tension and contraction twins, which occur on the $\{10\bar{1}2\}$ and $\{10\bar{1}1\}$, respectively. Like the names suggest, tension twinning occurs when the applied loading results in an extension in the c-axis, while a contraction twin occurs when there is a contraction in the c-axis. To satisfy von Mises′ criteria, twins of the $\{10\bar{1}2\}$ type may supply the missing deformation components.

2.3 Fatigue Overview

A large majority of structures and machine parts that fail during service has been attributed to fatigue failure. The American Society for Testing and Materials (ASTM) defines fatigue as the process of progressive changes of the materials properties during repeated application of stresses or strains, which leads to crack formation or failure [13]. During fatigue, damage to the material is accumulated through the repeated application of the stress cycles. Fatigue damage is also cumulative through the materials life. Fatigue failure can occur at stresses within the elastic region, resulting in catastrophic failure without any indications. Under a monotonic load of the same stress level, the material will not fail.

There are many factors that affect the fatigue life of a material. Primarily, they include:

- Loading Conditions – The stress state of the material, such as the stress amplitude and mean stress.
- Surface Quality and Geometry – Notches and/or variations in the surface roughness along the sample leads to stress concentrators, where crack initiation can occur during loading.
- Material History – Fatigue life varies from material to material, depending on the materials history and nature. Materials that are heat treated have internal defects, or residual stress will alter fatigue life.
- Environment – The surrounding temperature or a corrosive environment will vary fatigue life.

2.3.1 Stress-Based Fatigue Analysis of Crack-Free Components

Fatigue analysis can be conducted under the conditions of stress-controlled or strain-controlled tests. The earliest method to analyze the fatigue behaviour of materials was based on stress-controlled fatigue tests [14]. During stress-controlled tests, a cyclic stress is applied to the sample until failure occurs, which may occur at varying number of cycles depending on the magnitude of the stress applied. For low cycle fatigue, the applied stress is greater than the yield strength of the material and plastic deformation occurs during every cycle. Fatigue damage due to the plastic deformation accumulates in the microstructure and the material fails at a low number of cycles, typically $< 10^4$ cycles. For high cycle fatigue, the stress applied is typically less than the yield strength of the material, in the elastic region, and lasting for $> 10^4$ cycles.

For stress-based fatigue analysis, a fully reversed loading cycle is commonly used in a sinusoidal stress profile, where a material is stressed equally in tension as in compression in one cycle. In this loading case, the maximum and minimum stress applied are equal and with zero mean stress, the resulting stress ratio is -1. In these tests, a hysteresis loop is obtained which resembles information pertaining to the loading cycle and mechanical behaviour of the material. Perfectly elastic materials have an ideal linear stress-strain behaviour, and a cyclic stress generates a cyclically variable strain that is also in phase with the stress in these materials [15]. During loading, the materials absorb elastic energy under the cyclically stress, therefore, the unloading curve is always located underneath the loading curve [15]. The stress applied is assumed constant because the cross-sectional area of the sample theoretically does not change during loading. Under stress-controlled loading, the fatigue endurance limit of a material is mainly influenced by the material′s strength [8].

2.3.2 S-N Curves

The first systematic analysis of fatigue was conducted by August Wohler, who has been referred to as the father of systematic fatigue, for his work on the failure of railway axles during the mid-19^{th} century [16]. The fatigue tests of crack-free components under stress control yields information that can be plotted on a stress applied, σ_a, versus the number of cycles to failure, N_f. Almost always, a logarithmic scale is used for the number of cycles to failure. These plots are referred to as S-N diagrams or Wohler curves.

An S-N curve is constructed by testing a number of samples, usually $6-12$, at varying stress amplitudes and recording the number of cycles until failure [8]. There is a considerable amount of scattering in fatigue data, even if the samples are meticulously machined to the same dimensions and out of the same lot of materials used. Microscopic changes in the material can vary the fatigue behaviour of samples, even if they are tested at the same stress. From the obtained S-N curve, the endurance limit of the material can be found. The endurance limit, or the fatigue limit, is defined as the stress amplitude at which a material can theoretically survive an infinite number of cycles. Some materials have a well-defined endurance limit, while others do not. Thus, the stress amplitude at which the material survives 10^7 cycles is to be identified as the endurance limit.

2.4 Fatigue Failure Mechanism

The life of a material that failed due to fatigue can be divided into three parts:

i.) Crack Initiation

ii.) Crack Propagation Stage 1 – Slow crack growth

iii.) Crack Propagation Stage 2 – Sudden propagation leading to fracture

The initiation stage represents a majority of the fatigue life of the material, up to 90% of the lifetime can be attributed to this stage [17]. During cyclic loading of a material, generally, a crack initiates at a stress concentrator. Usually, crack initiation occurs at the surface of the sample, with notches and/or surface discontinuity acting as stress concentrators. The crack initiation stage is associated with the formation of micro cracks as a result of cyclic loading that form a macro crack in the next stage.

Once a crack is initiated, the crack growth in cyclic loading occurs in a series of steps

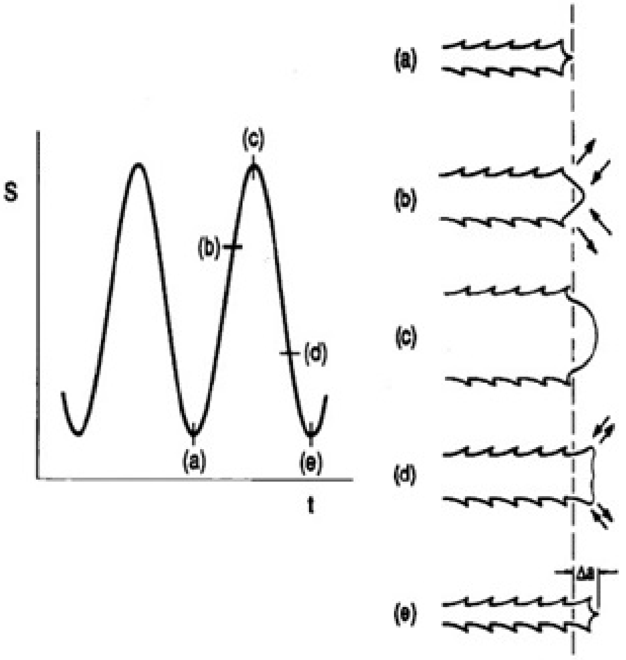

Figure 2.3: Laird′s fatigue crack propagation model [5].

through the opening and blunting of a crack tip. Crack growth occurs by a continual process of crack sharpening followed by blunting [8]. A representation of this process proposed by Laird is shown in Fig. 2.3 [5]. Under tensile loading, the crack is opened by normal stress and activates plastic slips at the tip into the virgin metal. At the highest point of loading, the crack tip blunts and has an increased radius. As the material undergoes the unloading part of the stress cycle, into compression, the crack tip closes, and the tip sharpens. After a complete cycle of loading and unloading, the crack has grown a certain distance. This process proposed by Laird, is referred to as plastic relaxation and is based on the notion that the plastic collapse of a crack occurs during the unloading and the crack tip closure phase leads to the tip concavity [5]. This step-by-step process leaves behind a footprint on the fracture surface, referred to as fatigue striations. Fatigue striations are microscopic details that cannot be seen with a naked eye and require the aid of a high-powered microscope, such as a secondary scanning electron (SEM) microscope, to view them. Frequently, visible examinations of the fracture surface of a fatigued material reveal a series of concentric markings referred to as ”beach” marks [8]. Unlike striations, beach marks are macroscopic in nature and can be seen with the naked eye. Beach marks are an indication of a change in stress during the fatigue process and may contain thousands of striations.

2.5 Fatigue of Pure Magnesium

Stevenson and Vander Sande cyclically deformed magnesium single crystals with a purity of 99.95%+ of differing orientations under strain-controlled fatigue tests [18]. They studied the correlation between fatigue life and slip behaviour of the differing crystal orientations, as well as strain amplitudes. With the use of TEM, they found that at low plastic strain amplitudes the deformation mechanism for magnesium single crystal tested was essentially single slip. While in high plastic strain amplitudes, evidence of duplex slip, which occurs when the material simultaneously slips on two or more planes, was observed. The duplex slip structure was observed in the orientations where single slip deformation is predominate in a tensile test. Also, twins were observed of the $\{10\bar{1}2\}$ type and were formed in the compressive half-cycle [18].

Yu and co-workers conducted fully reversed strain controlled cyclic tension-compression experiments on commercially pure polycrystalline magnesium, relating the fatigue damage developed to the cyclic deformation [19]. The fatigue tests were conducted at 1% and 0.12% strain amplitudes. Results showed that at a strain amplitude of 1%, the magnesium displays cyclic softening at the peak tensile stress but cyclic hardening at the peak compressive stress. While at 0.12% strain amplitudes, the stress-strain hysteresis loops show a cyclic hardening symmetry for both the tensile and compressive peak stresses. This behaviour however loosely correlated to the fatigue damaged observed for the varying strain amplitudes. At 1% strain, roughly 80% of the fatigue life is spent on initiating microcracks with minimal crack growth. The continuous initiation of microcracks was the reason for the cycle softening at the peak tensile stress. Whereas for a strain amplitude of 0.12%, fatigue life spent for initiating micro crack is roughly $50-70\%$. The microcrack initiation modes are highly dependent on the cyclic loading magnitudes. For the 1% strain amplitudes, massive tensions were formed due to the high degree of deformation. But for the 0.12% strain, the crack propagation is predominantly slip-induced [19].

2.6 Fatigue of Magnesium Alloys

Novy et al. conducted fatigue tests on extruded commercial AZ31, AZ80, and ZK60 magnesium alloys to determine the role of the microstructure on the fatigue crack nucleation and growth in the very high cycle region (VHCF) [20]. Fatigue tests were performed at an ultrasonic frequency with a load ratio of $R=-1$. The S-N curve for all three alloys showed a smooth transition to the VHCF ($N=10^{10}$) region which was not expected, usually, there are abrupt changes in the transition to this region. It was proposed that these smooth curves were as a result of the negligible influence of both the fatigue loading method and the frequency of loading on the fatigue life. Ultrasonic frequency was used for these experiments, which yields a different result for tests below $N<10^6$ in comparison to more conventional frequencies. In the AZ31 and AZ80 alloys, crack initiation occurred on the surface only, while in the ZK60 alloy there was evidence of both interior-induced and surface cracking initiation. In all the alloys, the S-N curves slightly decrease with an increasing number of cycles in the VHCF [20].

The study by Yin and colleagues examined the fracture morphology of a wrought commercial magnesium alloy containing Mg-3%Al-1%Zn [21]. The low-cycle fatigue properties of the material were investigated using a constant plastic strain amplitude controlled tests. Their results showed that the fracture morphology could be characterized by two regions. The first, a lamellar structure in the crack initiation and propagation zone as a result of twinning. As well as, a distinct dimple structure in the final rupture zone mainly due to slip. Another key observation is the evidence of twinning-detwinning occurring alternatively during the fatigue process. The compressive loading promoted twinning, while the tensile loading favored the detwinning process [21].

Morita et al. evaluated the cyclic behaviour in compressive and tensile loading-unloading conditions of extruded AZ31B magnesium alloy [22]. An S-N curve representing fatigue behaviour of the material was constructed under axial load-controlled conditions. The curve had a noticeable sharp bend, and the material had a well-defined fatigue limit of 90 MPa. This result was also shown by Tokaji et al. [23], Nan et al. [24], and Tsujikawa et al. [25]. Fracture analysis suggested that the fatigue crack initiation at the specimen surface, regardless of the stress amplitude applied. This result correlated with the findings by Novy et al. [20], as well as many other papers. The stress-strain hysteresis loops show a known anisotropy behaviour attributed to magnesium, but they also showed complicated pseudoelastic deformations both in tension and compression at varying stress amplitudes. At stresses above the fatigue limit ($>$ 90 MPa), deformation twins were evident in the microstructure that was recognized as of the $\{10\bar{1}2\}$ type by Tsujikawa et al. [25]. However, samples analyzed from the fatigue limit showed the presence of free deformation twins [22].

In addition, Nan and colleagues conducted studies on the fatigue behaviour of extruded magnesium AZ31 alloy under stress-controlled rotating bending tests in air [24]. Material characterization showed two types of lamellar structures, parallel to the extrusion direction, present in the microstructure. The first, known as phase A is the magnesium matrix, and the second is phase B which consisted of $Mg_{32}(Al,Zn)_{49}$. Phase B consists of a third distinct phase, referred to as phase C which is comprised of $Mg_{17}Al_{12}$ precipitates. From the fatigue testing, the S-N curve shows a sharp bend in fatigue life leading to a well-defined fatigue limit at 120 MPa. From their research, they discovered that the fatigue crack generates in phase C, in the early stages of fatigue and propagates through phase B. They attributed the sharp bend in the S-N to crack arrest in phase B. Hardness profiles of the phases show that the hardness in phase B is greater than phase C. Thus, it is difficult for the crack to grow with a low applied stress [24].

Similarly, in a study conducted by Tokaji et al., the fatigue behaviour and fracture crack propagation of rolled magnesium AZ31 under axial stress control with a stress ratio of -1 [23]. The S-N curve presented shows a bend in the fatigue data, with a well-defined fatigue limit at 50 MPa. Fatigue failure did not occur at this stress amplitude. However, there was evidence of non-propagating cracks observed on the specimen surface. Their study also showed evidence of a change in fracture modes in the S-N curve. Samples tested above 70 MPa, had fatigue cracks initiating on the surface at early stages of fatigue failure, mainly due to cyclic slip deformation. But, samples tested below this stress amplitude had subsurface fracture occurring, where facets were present at the initiation sites [23].

The cyclic fatigue behaviours of extruded magnesium AZ31 and AZ80, together with magnesium AZ91 and AE42, under axially loaded strain-controlled conditions, were studied by Zenner and Renner [26]. In regards of the AZ31 and AZ80, their results showed a pronounced anisotropy in the alloys on the material strength in comparison to the tensile and compressive loading conditions. The effect was more pronounced in the case of the AZ80 compared to the AZ31. Zenner and Renner hypothesized that the likelihood of twin formation as a function of the stress direction is the cause of the asymmetry of the deformation behaviour exhibited [26].

2.7 Friction Stir Welding

Friction stir welding (FSW) is a relatively new welding technique invented at The Welding Institute (TWI) of the United Kingdom (UK) in 1991 [3]. It is a solid-state joining technique, initially used to extend the weldability of aluminum alloys. Before FSW, some aluminum alloys were difficult to join due to cracking and porosity issues, however, since the invention of FSW its use has been extended to magnesium alloys, titanium alloys, and steels [3].

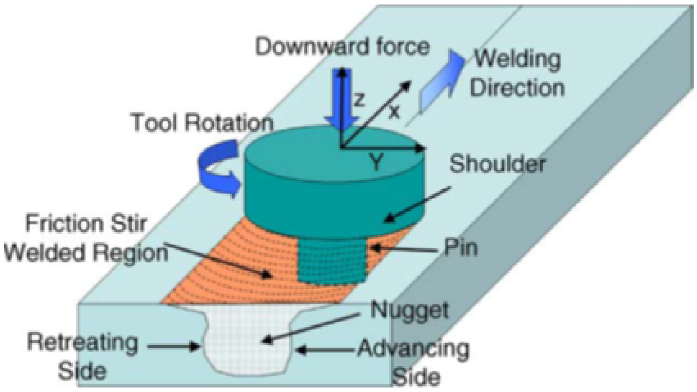

Figure 2.4: Schematic drawing of friction stir welding [3].

A non-consumable tool with a pin and shoulder is rotated at high speeds and is inserted into the material to be joined and moved along the intended joint. The tool serves two functions; the heating of the workpiece, as well as the mechanically stirring the material. The rotating shoulder and pin used to provide the necessary frictional heat to the local area around the workpiece to soften the material. The combination of the tool rotation and translation leads to the mechanical stirring of the material from the front of the pin to the back. A schematic of the FSW process is shown in Fig. 2.4. During the FSW process, the localized material around the material undergoes severe plastic deformation at elevated temperatures. However, FSW is referred to as a solid state joining technique because the temperature during the process stays below the melting temperature of the materials being joined. This process results in a fine and equalized recrystallized microstructure which produces good mechanical properties, in comparison to other joining techniques [3]. A summary of the metallurgical, environmental, and energy benefits of FSW is outlined in Table 2.3. FSW has been deemed the most significant development in metal joining in the past decade and is also referred to as a green technology due to its environmental and energy benefits in comparison to other conventional welding methods [3].

Morishige et al. examined the joint efficiency of A5052-H aluminum alloy and extruded AZ31B magnesium alloys [27]. The mechanical properties of the dissimilar weld were primarily dominated by the distribution of Al-Mg intermetallic compounds. In their first tests, the heat input rate during welding was too high, which resulted in a large number of these intermetallic compounds to form. However, to improve joint efficiency, it was suggested by the authors that the heat input rate must be lowered to suppress the formation of the Al-Mg intermetallic phase, particularly the $Al_{12}Mg_{17}$, as well as, finely disperse the compounds throughout the material [27].

The anisotropic effect of the material arrangement of dissimilar magnesium friction stir welds from the view point of microstructure and mechanical properties was investigated by Liu et al. [28]. They evaluated the properties of welds that were produced when extruded AZ31 alloy and AZ80 alloy are taken as the advancing side, respectively. Microstructure observation of the welds shows that even for the FSW of the same material, the material flow from the advancing side to the retreating side of the weld was more fluent, than that from the retreating side to the advancing side. The AZ80 alloy has a higher aluminum content, which attributes to the alloys higher strength and hardness, but lower ductility in comparison to the AZ31 alloy. When the AZ80 alloy was taken as the retreating side, the poor deformation of the AZ80 alloy leads to the hindered flow back of material to the

Table 2.3: Key benefits of friction stir welding [3].

Metallurgical Benefits	Environmental Benefits	Energy Benefits
Solid phase process	No shielding gas required	Improved materials use allows reduction in weight
Low distortion of workpiece	No surface cleaning required	Only 2.5% of the energy needed for a laser weld
Good dimensional stability and repeatability	Eliminate grinding wastes	Decreased fuel consumption in light weight aircraft, automotive, and ship applications
No loss of alloying elements	Eliminate solvents required for degreasing	
Excellent metallurgical properties in the joint area	Consumable materials saving	
Fine microstructure		
Replace multiple parts joined by fasteners		

advancing side of the AZ31. Thus, their satisfied joints consisted of AZ80 alloy at the advancing side and the AZ31 alloy at the retreating side [28].

2.8 Fatigue of Friction Stir Welded AZ Magnesium Alloys

Yang et al. studied the low-cycle fatigue behaviour of friction stir welded magnesium AZ31 alloy at a low and high rotation rate under strain control fatigue tests [29]. Their objectives were to explain the cyclic deformation characteristics of the FSW joints, as well identify the microstructural evolution during the cyclic deformation. They found that at any given strain amplitude, the FSW joints had a lower stress amplitude, a higher plastic strain, and a lower fatigue life than the base metal. This effect was more pronounced in samples that were tested at a higher strain amplitude. At low strain amplitude, twins of the $\{10\bar{1}2\}$ type was observed only in the nugget and thermal mechanically affected zone boundary. These twins were activated along this boundary and propagated to the nugget zone interior. Fatigue cracks initiated at the bottom of the FSW joints and propagated along the NZ/TMAZ boundary, where the $\{10\bar{1}2\}$ twins were observed [29].

Chowdhury et al. reported that the fatigue strength of FSW magnesium AZ31 alloy joints was affected by the pin thread orientation [30]. They conducted load-control fatigue tests on AZ31 base metal, as well as, FSW AZ31 samples. Their respective S-N curves were obtained. It was found that at high stress amplitudes, all the FSW joints had a lower fatigue life in comparison to the base metal. However, it was evident from their obtained S-N curve that this difference in fatigue life lessened as the stress amplitude decreased. Also, the fatigue limit of the FSW joints was lower by 20% for the left-hand threaded pins, and 40% for the right-hand threaded pins, in comparison to the fatigue limit of the base metal [30].

Padmanaban and Balasubramanian analyzed the effect of FSW parameters on tensile properties of magnesium AZ31 alloy joints, as well as the fatigue properties of the welds fabricated from the optimized conditions [31]. They conducted constant amplitude loading fatigue tests with a stress ratio of 0.1 at five different stress levels. They found that the fatigue strength of the base metal is 72 MPa but for the FSW AZ31 it was 51 MPa, this was a 29% reduction in fatigue strength as a result of the welding. SEM analysis of the fracture surfaces shows elongated dimples for the base metal, while the dimples were finer for the weld. TEM observation shows finger magnesium grains and $Al_{12}Mg_{17}$ precipitates compared to the base metal [31].

The fatigue of welded magnesium alloy joints was investigated by Tsujikawa et al. [25]. They examined the fatigue strength of friction stir welded extruded AZ31 and AZ61 magnesium alloys, under load-controlled fatigue tests with a stress ratio of 0.1. Their fatigue tests show a fatigue strength of 94.5 MPa and 105.5 MPa, for the base metal AZ31 and AZ61 respectively. However, when these materials were FSW, there was a drop in the fatigue strength of the joints. For the AZ31 joint, the fatigue strength is 75 MPa, while for the AZ61 the fatigue strength is 55.6 MPa. The drastic drop in fatigue strength for the AZ61 joint can be related to the joint efficiency for the weld which was found to be 53%, while the joint efficiency for the AZ31 joint is 78%. SEM analysis of the fracture surfaces showed evidence of fatigue cracks initiated at the center of the weld line, where the thickness of the sample is the smallest. Also, basal plane textures and flow patterns in the FSW affect the fatigue crack propagation in the magnesium alloys [25].

2.9 Finite Element Analysis of Rim Geometry

The investigation of the stress distribution on a vehicle rim was investigated in the early stages of the project. The finite element analysis of a wheel geometry for a prototype wheel was completed to determine the points of the rim that experience the highest stress levels during operation. Ju et al. investigated the stress for a prototype wheel fitted with a rubber air tire and exposed to a 800 kgf load by bearing contact in the hub. It was determined that the peak von Mises$'$ stress experienced by the rim is 21.45 MPa located at the rim section of the wheel near the hoop and spoke joint, as seen in Fig. 2.5. While the other sections experienced moderately lower stress than the peak, ranging from 14 – 18 MPa [6].

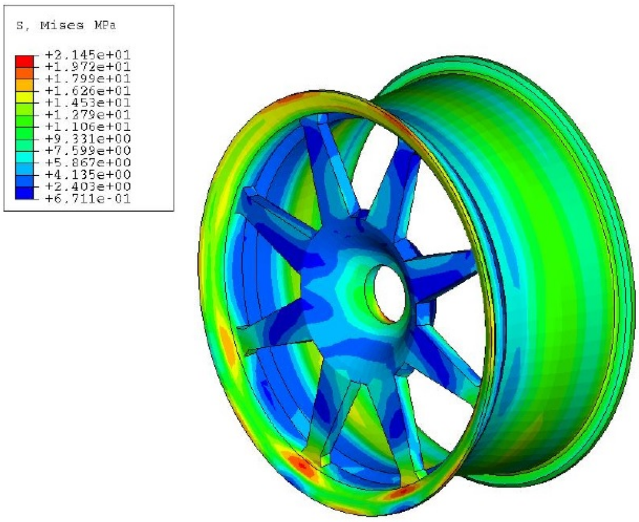

Figure 2.5: Finite element analysis of wheel with the geometry shown [6].

On the other hand, Praveen and Gopichand investigated the optimum geometric shape and alloy for the rim of a 4-wheel vehicle using finite element analysis. In their work, they investigated 4 different types of geometric shapes, H-type cross member, inclined cross member, straight cross member, and Y-type cross member. They used a more realistic load which included the weight of the vehicle, five passengers, as well as luggage. Their results showed peak stresses of 20 – 25 MPa located primarily at the point of contact between the hoop and rubber tire. While the other sections of the rims experienced moderate stresses below the peak stress levels [32].

Chapter 3

Experimental Procedure

3.1 Material Characterization and Welding Parameters

In the present study, the materials under investigation were friction stir welded (FSW) magnesium alloys; more specifically, extruded commercial alloys AZ31 and AZ61 welded to extruded AZ80. Their chemical compositions are outlined in Table 3.1, with magnesium to balance. The shoulder and pin used for FSW are made of H13 carbon steel, and the pin specifications are 4.5 mm long, M6 thread, 15 mm shoulder, flat taper. The parameters used for the friction stir welding are outlined in Table 3.2.

Table 3.1: Chemical composition of magnesium alloys used.

Alloy	Elements (*wt%*)									
	Al	Zn	Mn	Si	Pb	Zr	Cu	Fe	Ni	Be
AZ31	2.67	0.77	0.32	0.01	< 0.01	< 0.01	< 0.005	0.004	< 0.002	< 0.0005
AZ61	7.12	0.42	0.35	0.02	< 0.01	< 0.01	< 0.005	< 0.003	< 0.002	< 0.005
AZ80	8.77	0.44	0.19	0.02	< 0.01	< 0.01	< 0.005	< 0.003	< 0.002	< 0.0005

Table 3.2: Welding parameters for the dissimilar welds, courtesy of Dr. Adrian Gerlich.

Weld Designation	Rotations per minute (RPM)	Speed (mm/min)	Rotation	Retreating Side (RS) Material	Advancing Side (AS) Material
32	900	89	CCW	AZ31	AZ80
33	900	89	CCW	AZ61	AZ80
37	900	63	CCW	AZ61	AZ80
38	900	63	CCW	AZ31	AZ80

In all the welds, the advancing side is AZ80, while the retreating side was comprised of AZ31 and AZ61. The orientations of the materials on the weld chosen are a result of findings in literature [33][34][35]. Where it was found that the weakest part of the weld is the interface between the base metal and advancing material. This interface was placed in the gage length of the fatigue specimens, leaving the weld centre-line at the fillet and mostly the retreating side material (AZ31/AZ61) in the grip region. The advancing side in the FSW process is where the solid material starts to transform into a semi-solid due to the friction from the pin and shoulder. This semi-solid begins to flow around the tool pin plunged into the material. Thus, the advancing side during FSW generates a higher friction stress and more heat causing an asymmetric weld regarding various properties. All the welds were produced at the University of Alberta.

An AZ80/AZ31 weld fatigue specimen was examined along the weld using an optical microscope. The specimen was mechanically ground using 1200, 2400, and 4000 SiC grit along the axial direction, followed by polishing using 6 μm, 3 μm, and 1 μm water-free diamond suspension. For the observation of the weld regions under an optical microscope,

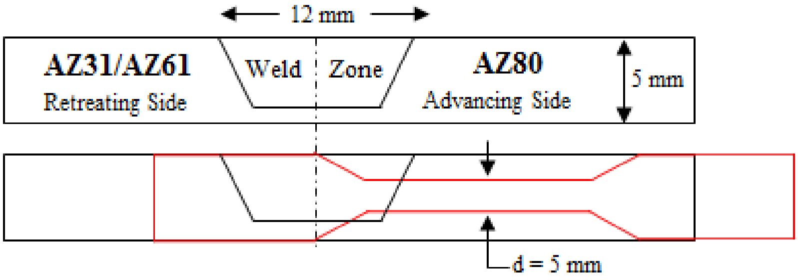

Figure 3.1: Fatigue specimen orientation with respect to friction stir welding of materials.

the specimen was etched for 30 seconds with 1 g tartaric acid and 20 mL water. Immediately after etching, the specimen was placed under running water for 60 seconds. This etching process reveals the AZ80 portion of the weld located in the gage length.

Grain size measurements along the weld were performed using the lineal intercept method, as outlined in ASTM E112 [36] and shown in Eq. 3.1.

$$N_{100x} = 2^{G-1} \tag{3.1}$$

Where N is the number of grains in a 1 in^2 area at 100x magnification and G is the ASTM grain size number [36]. A total of three different fields were analyzed to achieve an average value for the sections of the weld.

3.2 Sample Geometry

To conduct the fatigue experiments, the welded material was machined into cylindrical fatigue specimens with an orientation shown in Fig. 3.1. The samples were welded from 5 mm thick plates and were machined from the center of the welds to eliminate the effects of surface defects as a result of the FSW. The shape and dimensions of the specimens used for the stress controlled axial fatigue tests are shown in Fig. 3.2, in accordance with ASTM

E8 standards. The length of the specimens are 58 mm and the diameter of their necks are 3.5 mm. The transition from the grip section to the gage is machined as a gentle curvature to avoid any sharp changes in thickness, to avoid any stress concentrators that would alter the results. All the machining of the specimens was done at Queen′s University.

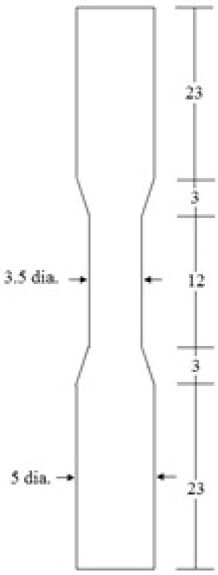

Figure 3.2: Shape and dimensions of the fatigue specimens in millimeters.

3.3 Surface Roughness Observation

In the previous chapter, it was mentioned that surface roughness is one of the factors that affect the fatigue life of a material. After the base materials were friction stir welded, they had been machined into fatigue specimens. The machining process left markings on the surface that would affect the fatigue life of the material. A preliminary investigation of the effect of surface roughness on the fatigue life of the specimens was conducted.

Surface roughness measurements were taken using the Zygo NewView 5000 at the Mc-

Master Manufacturing Research Institute (MMRI) facility. The Zygo machine, shown in Fig. 3.3, is a non-contact $3-D$ surface profiler that scans the specimen with light interferometry to image and measures the topography of the surface. With the specimen orientated horizontally, an area of 6 mm x 0.4 mm, x and y respectively, was observed. Since the Zygo machine uses light to scan the surface, the nature of the cylindrical specimens does not allow light to be reflected back to the detector which skewed the results obtained. To counteract this problem, a filter was available in the program to remove the outer edges and assume a rectangular surface. After the data is collected, a 3-dimensional surface topography image is obtained, as well as the average surface roughness, R_a.

Figure 3.3: The Zygo NewView 5000 surface profiler machine [7].

The specimens had artifacts of the machining on the surface, which may act as stress concentrators during testing, on the gage length. Due to the cylindrical shape of the specimens, the surface of the gage was manually polished using a lathe and 600 grit SiC to smoothen the surface. Throughout the polishing procedure, the diameter of the gage was measured multiple times to avoid any sharp changes in the cross-section.

3.4 S-N Fatigue Testing Set-Up

All fatigue testing was performed on an MTS-858 servo-hydraulic table-top tensile testing machine equipped with a Test Start IIs controller.

Prior to fatigue testing, the diameter and gage length of the specimen was measured using a digital caliper. The specimen was placed in a grooved channel to help avoid any unnecessary contact between the caliper and specimen surface. The diameter of the specimen was measured multiple times along the gage length if there were any discrepancies the smallest value would be chosen and marked with a fine-tip marker. These are measurements required by the fatigue program to complete necessary calculations post-testing. The measured diameter values allow for the calculation of the cross-sectional area, and the desired applied stress will give the resulting applied loads.

After the measurements and calculations had been completed, a MTS 1385314 extensometer was attached to the specimen using dental elastics. The extensometer was attached very carefully to avoid significant contact between the teeth and the specimens gage, which may cause scratches to form on the surface. Two dental elastics were used to allow the extensometers teeth to measure parallel to the tensile load applied independently of each other.

At this point, the HSM and HPU were turned on, as well as the MTS controller which relays information from the mechanical testing apparatus to the computer program. The control mode was set to Displacement Control which implies that the hydraulic grips are controlled by the distance between them. The specimen, with the extensometer attached, is loaded into the top grip first. The grips were closed slowly to avoid any cracking of the specimen in the grips. The top grip is then lowered using the Displacement Control such that the specimens bottom grip lines up with the bottom grip of the machine. The control mode is now switched to Force Control, which implies that the grips will adjust themselves if a certain threshold force is exceeded. Again, the grips are closed slowly. Once the specimen is mounted the offsets, pertaining to displacement, force, and strain are all set to 0.

The fatigue program used has actions that the program conducts when limits are exceeded during testing. One of the more important actions is identifying when the sample fails so the machine stops conducting the fatigue test. If the distance between the upper and lower grip surpasses 12.50 mm, the program will hold. At this point, the grips will stay apart, and the number of cycles will not continue counting. However, there is a possibility that after fracture, the next stress cycle applied may have resulted in the fracture surfaces coming into contact with each other.

3.5 Fatigue Test Specifications

The specimens were subjected to a stress-controlled, fully reversed sinusoidal stress profile. The fully reversed profile implies that the stress ratio, $R = -1$, and the mean stress, (σ_m), is also 0 MPa. The MTS fatigue system has a ramp period from the first to the tenth cycle to reach the stress amplitude input. A frequency of 4 Hz was found to be sufficient to avoid any slipping or overheating of the specimen. A representation of the stress profile is shown in Fig. 3.4. It is important to conduct the fatigue tests with the stress ratio chosen because it is known that due to the crystal structure of magnesium there is an asymmetry in the properties when it is subjected to tensile and compressive loads.

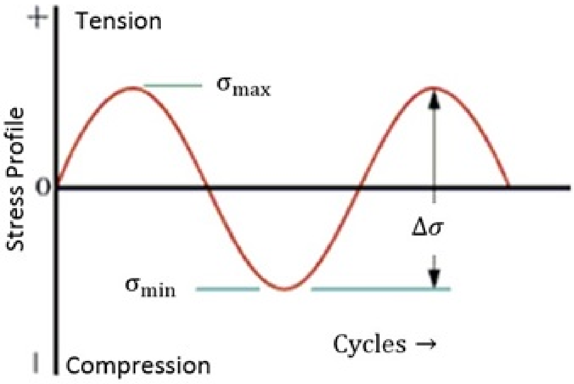

Figure 3.4: Fully reversed, sinusoidal stress profile schematic.

3.6 Sample Preparation for SEM and TEM Analysis

3.6.1 SEM Sample Preparation

Fracture surfaces from fatigued samples were analyzed using the JEOL-6610LV scanning electron microscope (SEM). Fracture surfaces from high and moderate stress amplitudes were cut from the shorter gage length. The remainder of the gage length was used for texture analysis and transmission electron microscopy (TEM) thin foils.

The primary limitation of SEM fracture analysis is the sample size. The fracture surfaces used were 3 cm in height to safely occupy the sample chamber in the machine. The fracture surfaces were cut through spark erosion cutting, using a dielectric oil submerged-sample spark cutter. Once the samples were cut, they were cleaned using acetone to remove any excess oil or contamination on the surface. The samples were mounted on a stub using double-sided carbon tape. An accelerating voltage of 5 kV and a working distance of 10 mm was used for observations.

3.6.2 TEM Sample Preparation

Transmission electron microscopy (TEM) was used to for a more in-depth analysis of the developed dislocation structure in the fatigued samples. TEM is a microscopy technique whereby a beam of electrons is transmitted through the material; this requires the sample to be very thin, essentially a thin foil. Three specimens were used for TEM observation with varying stress amplitudes and fatigue lives. The first sample had a stress amplitude of 150 MPa and lasted for 761 cycles, the second had a stress amplitude of 80 MPa and lasted for $18,815$ cycles, while the last sample had a stress amplitude of 70 MPa and run-out at $1.132E+7$ cycles. As previously mentioned, the remainder of the gage length after the fracture surface cut was used for TEM analysis. Approximately 500 μm slices were cut from the gage length using the same spark-erosion cutter used for the fracture surfaces. These slices were hand-thinned into foils, to a target thickness of $80-100$ nm by mechanical grinding using increasing grit of SiC sand paper with material removed from both sides of the slices. The foils were then punched to a diameter of 3 mm to fit in the TEM sample holder. After punching, the thin-foils were polished to a 3 μm finish using a water-free suspension as a lubricant.

TEM thin-foils were electropolished to electron transparency using Struers TenuPol-5 twin-jet and a 90 V applied voltage. The solution used contained 22.3 g $Mg(ClO_4)_2$, 10.6 g $LiCl$, 200 mL butyl cellosolve, and 1000 mL ethanol, and was cooled to 55°C using liquid nitrogen. TEM studies were carried out on the Philips CM12 electron microscope at the Canadian Centre for Electron Microscopy (CCEM).

3.7 Texture Measurements

The texture of samples for the 150 MPa, 80 MPa, 70 MPa (endurance limit) and undeformed samples were measured by X-ray diffraction (XRD) using a Bruker D8 Discovery diffractometer with a Co $K(\alpha_1)$ radiation source. The raw data frames were evaluated and incomplete pole figures for $\{0002\}$, $\{10\bar{1}0\}$, $\{10\bar{1}1\}$, and $\{10\bar{1}2\}$ was generated using Bruker General Area Detector Diffraction System (GADDS) V4.1.50. The raw data frames were also used for the MTex 3.5 texture software package using MATLAB as input files to produce calculated pole figures. Intensity correction, normalization of intensities, and data smoothing was performed on the raw data. Euler angles were used to generate orientation distribution functions (ODF) and recalculated pole figures were also produced.

Chapter 4

Results

4.1 Surface Roughness Measurements

A preliminary investigation of the effect that surface roughness has on the fatigue life of the friction stir welded specimens was conducted. The specimens had their surface roughness measured before and after lathe polishing, followed by fatigue testing. From the surface roughness data obtained, the program outputs a value for the average surface roughness, R_a, which includes missing data points. These missing data points are a result of sections of the specimens not reflecting light, possibly due to debris located on the surface. The average surface roughness before lathe polishing was found to be approximately $1.58 - 3.85\ \mu m$. While the average surface roughness after polishing is approximately $0.38 - 0.77\ \mu m$. The 3-dimensional oblique plots from the surface roughness data are shown in Fig. 4.1.

The surface finish is characterized by three components, i.) surface roughness, ii.) form, and iii.) waviness. Surface roughness is a measurement of the vertical variation of texture on a surface from its ideal form. The larger the deviations, the rougher the surface is. However, if these deviations are small, then the surface is considered smooth. The roughness of a surface may indicate the performance of a mechanical component; a rough

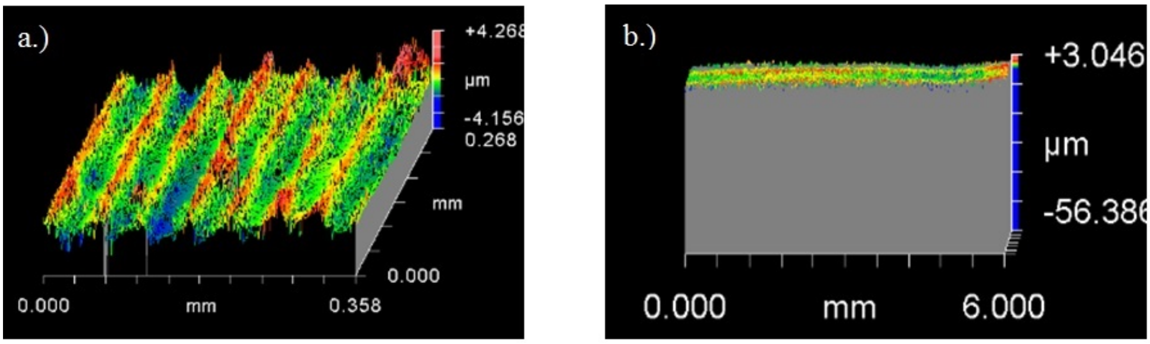

Figure 4.1: Surface roughness oblique plots, a.) before polishing, and b.) after polishing.

surface has many irregularities that can act as stress concentrators for crack nucleation and are more susceptive to corrosion in different environmental conditions. The form is the predominant surface pattern, while the waviness component is the global view of the surface features of the specimen. Surface roughness is undesirable in materials used for mechanical application because it is difficult to control. From Fig. 4.1, it is evident that before polishing the surface of the specimens have concentric machining marks, while these marks are removed after polishing. According to the software used by the Zygo NewView 5000, the surface roughness of the specimens before polishing was considered smooth because the concentric machining marks provided a certain form and waviness that did not deviate significantly. However, this result should not be accepted blindly as these machining marks resulting in sharp changes of the surface texture in localized areas on the specimens, which has previously been found to affect the fatigue life of the material.

Electrolytic polishing was considered as a method to remove these machining marks and provide a smooth surface for fatigue testing. Essentially, this polishing technique removes metal from the specimen through an anodic dissolution process, under optimum conditions. During electrolytic polishing, normally there is a plateau region on the respective current density vs. voltage plot where the current density does not change with voltage. In this region, electrolytic polishing of the material occurs, while anything before or after this region results in etching and pitting of the specimen, respectively. However, it is difficult to guarantee these optimum conditions because there are many factors that affect the quality of the surface such as; surface contact, the electrolyte used, temperature, time, voltage, stirring, the orientation of the anode and cathode, etc. These various factors increase the degree of difficulty to obtain a smooth and shiny electropolished surface.

In the present work, electrolytic polishing was conducted on a number of specimens using a variety of electrolytic solutions and conditions. The solution that worked the best contained 40% ortho-phosphoric acid and 60% ethanol operated at 30 V at room temperature. Although the electropolishing provided a smoother and shinier finish, there was evidence of pitting on the surface as a result of the polishing procedure. The average surface roughness values of these specimens ranged from approximately $0.9 - 1.5\ \mu m$. It was expected that the surface roughness of the specimens would be reduced. However, the Zygo Newview 5000 is a light profilometer which relies on using the light reflected back to the detector to analyze the surface. Therefore, the pits produced during the electropolishing do not reflect the light back to the detector, which results in the machine reading it as a zero or negative value.

Considering the negative effect that electrolytic polishing had, the remainder of the specimens were instead manually grinded with the aid of a lathe. Preliminary specimens were polished to a finish of 4000 SiC grit, however, this was very time-consuming and resulted in an undesired amount of material loss in the gauge length. Instead, the specimens were polished to a 600 SiC grit finish, which was deemed sufficient to remove the machining marks without reducing the cross-sectional area significantly. Also, using 600 grit SiC to mechanically polish the surface coincides with the experimental method proposed in several research papers in this area.

4.2 Weld Characterization

The optical micrograph in Fig. 4.2 shows a varying microstructure along the AZ80/AZ31 fatigue specimen. As expected in the geometric outline of the fatigue specimen previously shown, the stir zone between the AZ80 and AZ31 is located at the transition between the gage length and the grips. Using the lineal intercepted method, the ASTM number (*n*) for the AZ80 base material was calculated to be 6.537. Using Table 4 in ASTM E112-12 [36], the average diameter of the grains is approximately 39.93 μm. For the heat affected zone, the ASTM number was calculated as 8.295 and the average diameter of the grains is approximately 20.34 μm. Almost all the fatigue specimens tested failed at the interface between the base material and heat-affected zone. The sharp change of grain size may be an indication of a loss of ductility that allows for the stress applied to localize and facilitate fracture in the specimens. The nature of the FSW is asymmetrical because of the tool rotation and the difference in the heating effects experienced by the advancing and retreating side of the weld. Essentially, the retreating side of the material is stirred into the advancing side of the material. In the FSW process, the HAZ region does not experience any mechanical deformation from the shoulder or pin, but the region does undergo a thermal cycle due to the heat conduction produced. The temperature in the thermal cycle allows for dynamic recovery but not recrystallization. However, the base material region is not affected by the welding process, and the microstructure is ultimately unchanged from the starting material. The average grain size in the AZ80 base material is almost double that of the grains in the HAZ. The grains in the HAZ are relatively coarse in comparison to the other regions of the FSW, and it has been found that fracture tends to occur in this region.

The interface between the HAZ and AZ80 BM, where the grain size gradient is evident, is shown in Fig. 4.3. The microstructure of the weld shows a number of precipitates dis-

Figure 4.2: Optical Micrograph of AZ80/AZ31 FSW along the fatigue specimen.

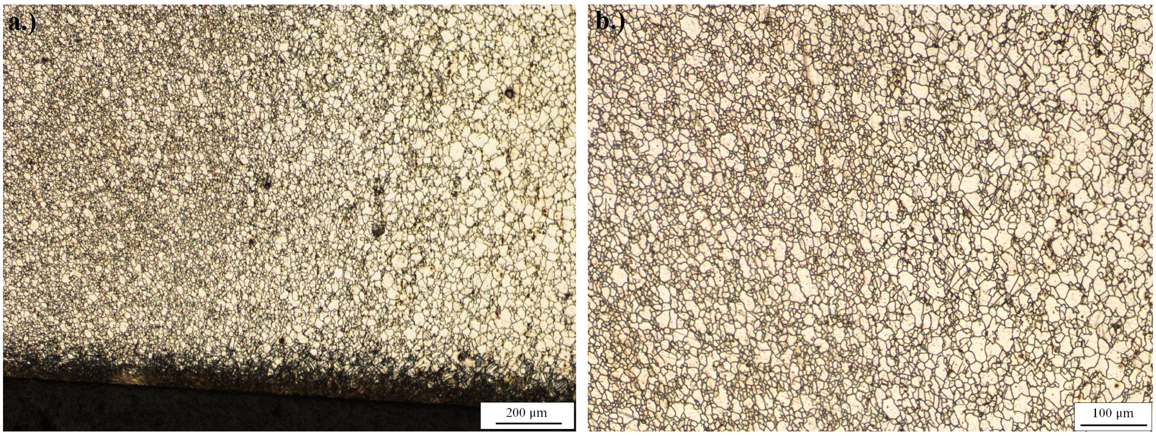

Figure 4.3: Higher magnification micrographs of AZ80/AZ31 FSW weld 32, a.) near the failure location at 50x magnification and b.) HAZ and AZ80 BM interface at 100x magnification.

tributed throughout the material, which are presumed to be $Mg_{17}Al_{12}$. This region contains primarily AZ80, which inheritably has a higher fraction of precipitates in the base material in comparison to AZ31 due to the increased aluminum content in the alloy. The HAZ has a lower number of these precipitates and is possibly due to the thermal cycling this region undergoes from the heat conduction produced in the FSW. During FSW, sufficient heat generation is required to achieve a stable material flow throughout the process with no defects or porosity in the weld. The heat generation produced during the weld may also result in the dissolution of the $Mg_{17}Al_{12}$ intermetallic compound in the material.

4.3 S-N Curves

Fig. 4.4 and Fig. 4.5 represent the S-N curves for weld 33 and weld 32, which correspond to the dissimilar welds of AZ80/AZ61 and AZ80/AZ31, respectively. As seen from both figures, there is an expected increase of fatigue life with decreasing stress amplitudes. It has been documented that some materials, including the magnesium alloys in the present work, experience a sharp bend in the S-N curves. For materials that do not have a well-defined endurance limit, the general rule is defining their endurance limit as the stress at which the material survives 10 million cycles. The sharp bend in weld 33 occurs around a stress amplitude of 90 MPa, while in weld 32 it occurs around a stress amplitude of 70 MPa.

As seen from Fig. 4.5, at a stress amplitude of 70 MPa weld 32 had a fatigue life in excess of 1.13×10^7 cycles, while at a stress amplitude of 80 MPa it is $32,016$ and $18,815$ cycles. A difference of 10 MPa in the stress amplitude resulted in a significant shift in the fatigue life; an increase upwards of 600 times. Accordingly, a sharp bend is observed in the S-N curve. It is noteworthy, that after a month of testing the specimen at a stress amplitude

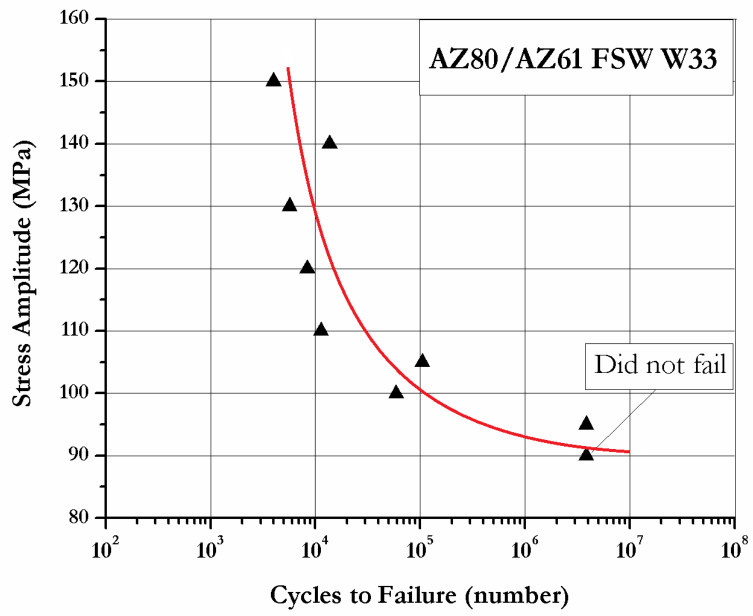

Figure 4.4: S-N curve for weld 33 of FSW magnesium AZ80/AZ61.

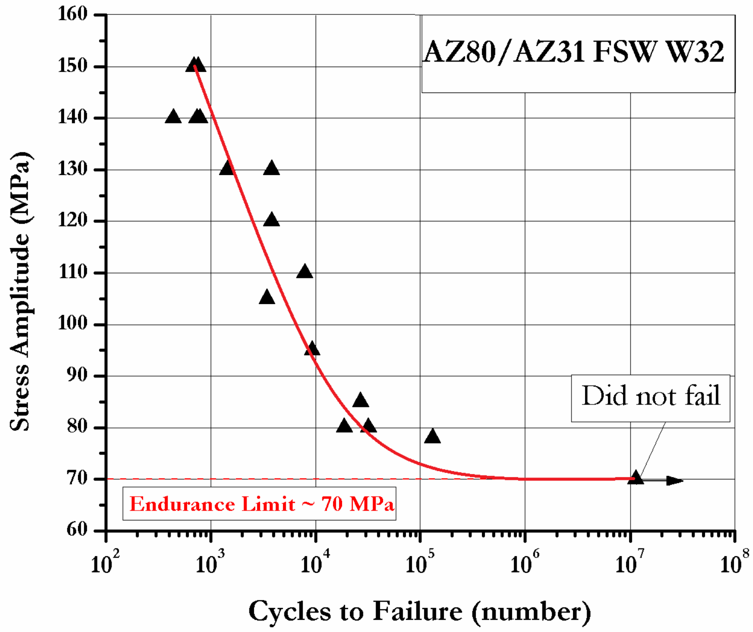

Figure 4.5: S-N curve for weld 32 of FSW magnesium AZ80/AZ31, with the endurance limit shown.

of 70 MPa did not fail. Since the specimen satisfied the endurance limit requirement, the test was terminated. Similar behaviour is seen in the fatigue data for the AZ80/AZ61 weld, shown in Fig. 4.4. The fatigue life at a stress amplitude of 90 MPa had a fatigue life of 3.83×10^6 cycles, while a specimen tested at 100 MPa had a life of $59,096$ cycles, resulting in a sharp bend occurring at 90 MPa. None of the specimens tested for this weld met the requirement of fatigue life for the endurance limit stress, therefore, the endurance limit for this weld was not found experimentally. This was primarily due to a lack of specimens available to continue testing. Nonetheless, the data in Fig. 4.4 suggest that the endurance limit should be somewhere in the range of $85 - 95$ MPa.

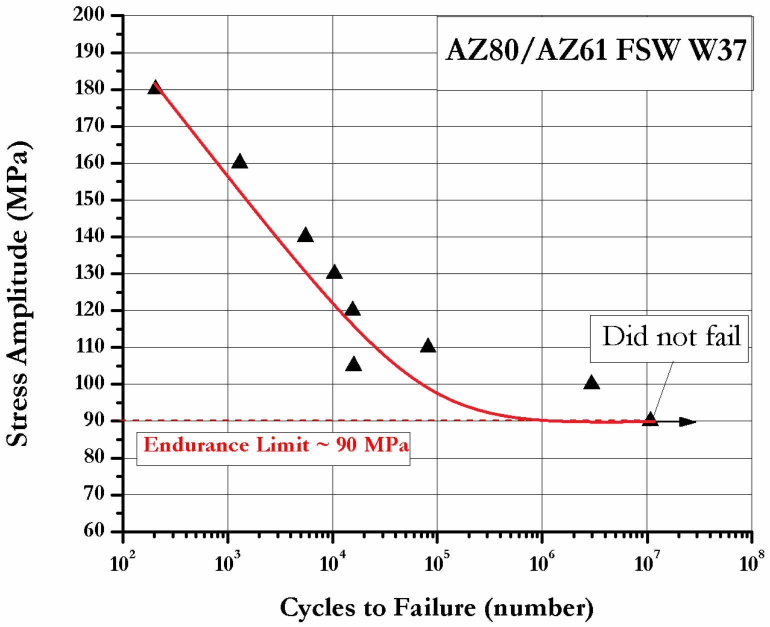

Figure 4.6: S-N curve for weld 37 of FSW magnesium AZ80/AZ61, with the endurance limit shown.

Fig. 4.6 and Fig. 4.7 represent the S-N curves for weld 37 and weld 38, which correspond to the dissimilar welds of AZ80/AZ61 and AZ80/AZ31, respectively. To recall, the

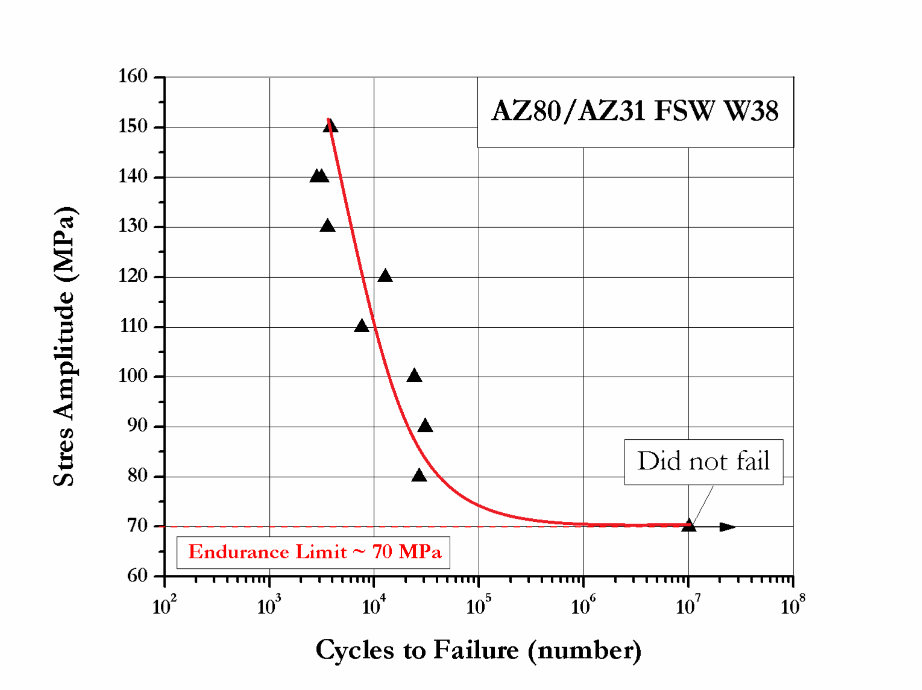

Figure 4.7: S-N curve for weld 38 of FSW magnesium AZ80/AZ31, with the endurance limit shown.

difference between these dissimilar welds is the speed at which they were produced at, for welds 32 and 33 the welding speed is 89 mm/min, while for welds 37 and 38 the welding speed is 63 mm/min. The fatigue behavior of these welds agree with the results found in the previous welds corresponding to the same materials used. Likewise, there is an expected increase in fatigue life with a decrease in stress amplitude with a prominent bend in the S-N curve evident in both welds. For the AZ80/AZ61 weld, the sharp bend occurs around a stress amplitude of 90 – 100 MPa, with an endurance limit of 90 MPa.The specimen tested at this stress amplitude had a fatigue life in excess of 1.069×10^7 before the test was terminated. The previous S-N curve for the other AZ80/AZ61 weld (weld 33) the endurance limit was not found due to an insufficient number of fatigue specimens available. However, it was estimated that the endurance limit would be in the range of 85 – 95 MPa, which agrees with the results found in Fig. 4.6. On the other hand, for the AZ80/AZ31 weld, the sharp bend occurs around 70 – 80 MPa with an endurance limit of 70 MPa. The specimen tested at this stress amplitude had a fatigue life in excess of 1.006×10^7 before the test was terminated. This result agrees with the previous S-N curve for the AZ80/AZ31 weld which also showed an endurance limit of 70 MPa.

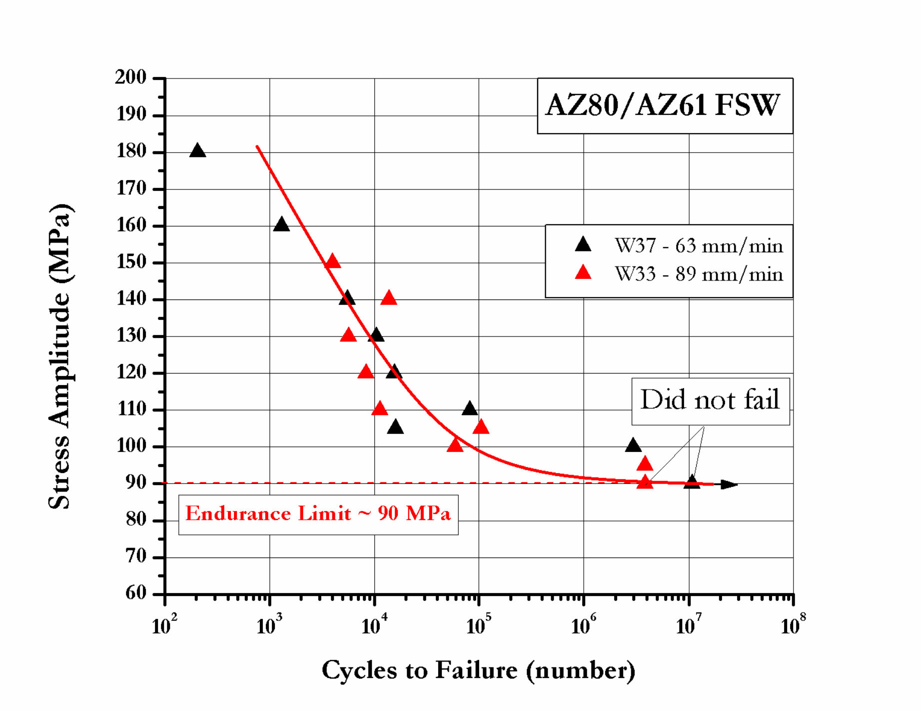

Figure 4.8: S-N curve showing combined fatigue data for the AZ80/AZ61 welds 33 and 37, with the endurance limit shown.

The combined S-N curves for the AZ80/AZ61 weld and AZ80/AZ31 are shown in Fig. 4.8 and Fig. 4.9, respectively. The fatigue data for each set of dissimilar welds show a good correlation with a similar trend observed in each curve. There is also a degree of reproducibility in the fatigue data even though S-N curves tend to have a large scatter in the data. The fatigue data in S-N curves tend to scatter the most at higher stress amplitudes, primarily because at high stresses the sensitivities to specimen preparation is significant. While at lower stress amplitudes, the scatter between the results is reduced. As expected

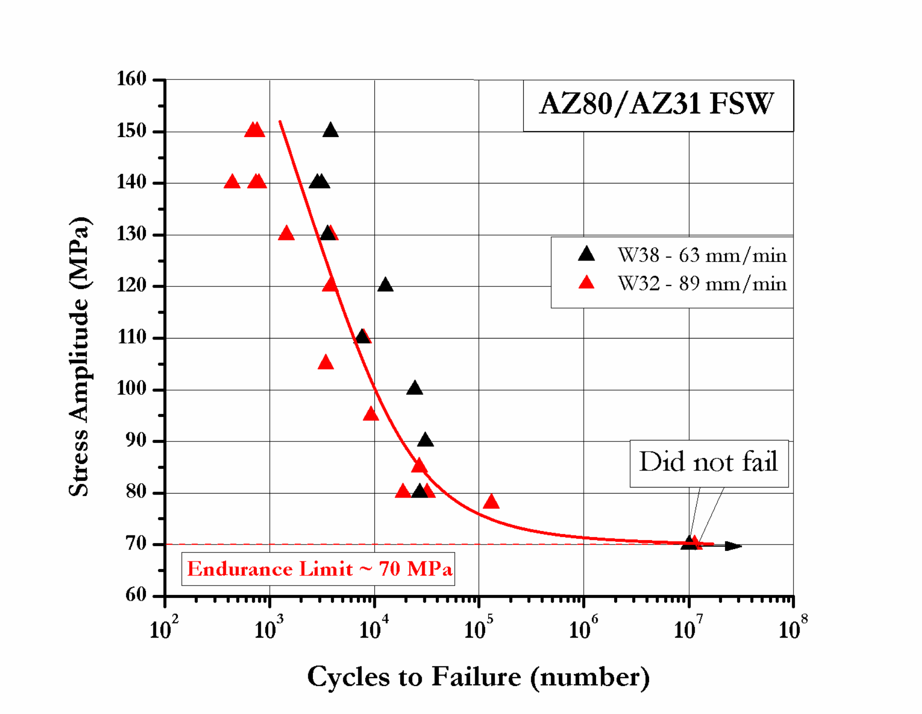

Figure 4.9: S-N curve showing combined fatigue data for the AZ80/AZ31 welds 32 and 38, with the endurance limit shown.

with S-N testing, there are some points from the fatigue results that do not match exactly, however, they still fall within a reasonable range.

A further analysis via SEM, TEM, and XRD was conducted for the AZ80/AZ31 weld 32.

4.3.1 Invalid Results

During fatigue testing, a number of specimens from both welds failed in the grip section and not in the expected gage length. Some of these failures occurred after a few hundred or thousand cycles, while others failed after millions. It was determined that these failures were occurring due to improper specimen mounting, as well as over-tightening due to a high grip pressure. To counteract these results, the grip pressure was reduced from 5 MPa to 3 MPa. Also, extra care was taken during mounting, ensuring the specimen was aligned parallel to the machine grips. A summary of these invalid results is shown in Table 4.1.

Table 4.1: Invalid test results for the S-N curve for both welds.

Weld Number	Stress Amplitude (MPa)	Cycles to Failure (number)
W33 - AZ80/AZ61	140	$183,246$
	108	$137,168$
	100	$216,821$
	95	$1,900$
	90	$285,245$
	90	1.87×10^6
W32 - AZ80/AZ31	76	5.12×10^6
	75	4.94×10^6

4.4 Mechanical Behavior

4.4.1 Tensile Testing Results

Tensile testing of three AZ80/AZ31 friction stir welded specimens was conducted prior to fatigue to experimentally find a value for the yield strength of the material. The specimens tested are identical to the specimens used for fatigue testing, both in dimensions and location of the weld within the specimen. The resulting tensile curves that were tested are shown in Fig. 4.10.

From the figure, it is apparent that two of the three curves had almost exact tensile behavior, while the third showed a slightly lower flow stress, but similar yield stress and

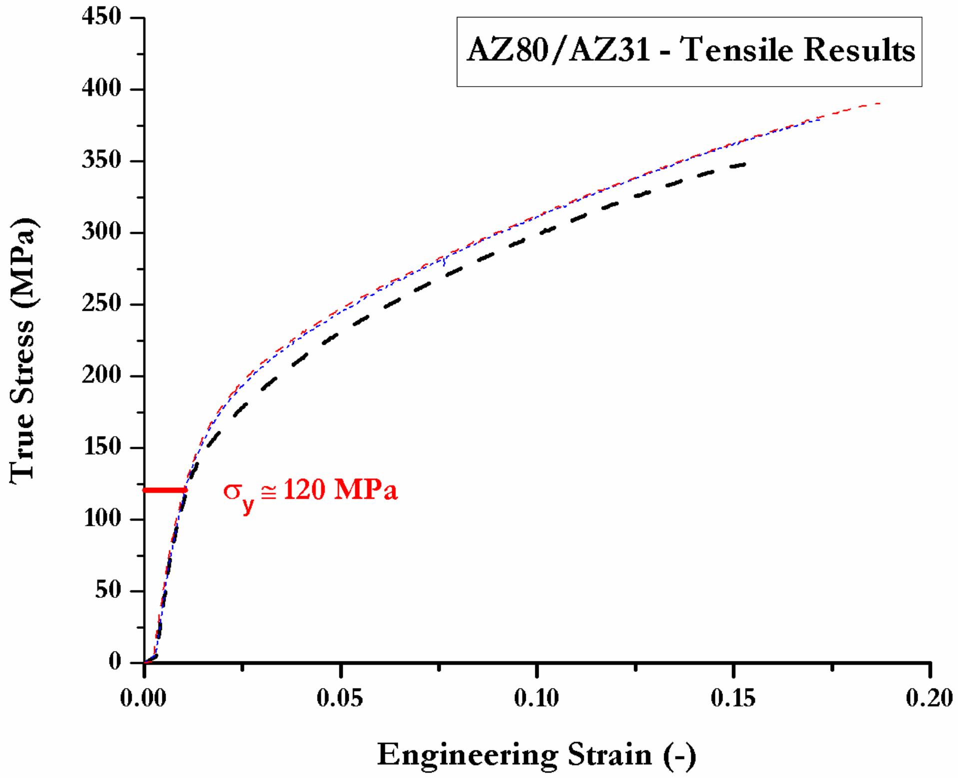

Figure 4.10: Tensile testing curves for weld 32 of FSW magnesium AZ80/AZ31.

work hardening rate during plastic region. The tensile curves do not show a distinct elastic to plastic region transition. The 0.2% off-set method was used to find the experimental yield strength of the friction stir weld which was found to be approximately 120 MPa. The tensile curves show a rounded and an extended plastic region where the material sustained plastic deformation before fracture occurred, suggesting that the material is ductile in nature. All three tensile samples failed in the region where the heat-affected zone (HAZ) of the friction stir weld meets the AZ80 base metal

4.4.2 Cyclic Stress-Strain Responses

When materials are subjected to cyclical loading that produces plastic strains, their mechanical behavior responses can be complex and may result in the formation of a hysteresis loop. The hysteresis curves for the 150 MPa, 80 MPa, and 70 MPa specimens are shown in Fig. 4.11. The first cycle, tenth cycle, and the mid-life cycle loops are shown in each figure for their respective fatigue specimen. The mid-life cycle stress-strain hysteresis loops for all of the specimens have a more pronounced Baushinger-life effect than the first cycle response, while the loops show the presence of asymmetry in the mechanical behavior. It is noticeably from the figures that the stress-strain hysteresis loops do not have the same maximum stress amplitude for the first cycle in comparison to the tenth and mid-life cycle curves. The MTS fatigue system used for testing requires 10 cycles to ramp up to the desired peak tensile stress amplitude imputed for the specimen. Therefore, the stress applied in the first cycle will not be the same stress amplitude that has been manually input. Furthermore, the calculated plastic strain vs. the number of cycles to failure was plotted for the 150 MPa, 80 MPa, and 70 MPa, specimens. The resulting plots are shown in Fig. 4.12.

For the 150 MPa specimen, the applied stress amplitude is above the experimental yield strength of the material, which was found to be 120 MPa. The first cycle shows a smaller hysteresis loop because the machine has yet to ramp up to the desired stress amplitude. The tenth cycle is the first cycle that the material undergoes the 150 MPa stress amplitude, and the result is a larger hysteresis loop. Since the stress applied is larger than the monotonic yield strength of the material it lies in the low-cycle regime, where fatigue testing generally lasts $< 10^4$ cycles. Out of the three cycles plotted, the tenth cycle has the largest amount of inelastic strain. The inelastic strain, or plastic strain, results in the permanent deformation which is not recovered upon unloading of the specimen. At 400 cycles, the plastic strain the specimen experiences decrease as the material begins to work hardening each cycle lead-

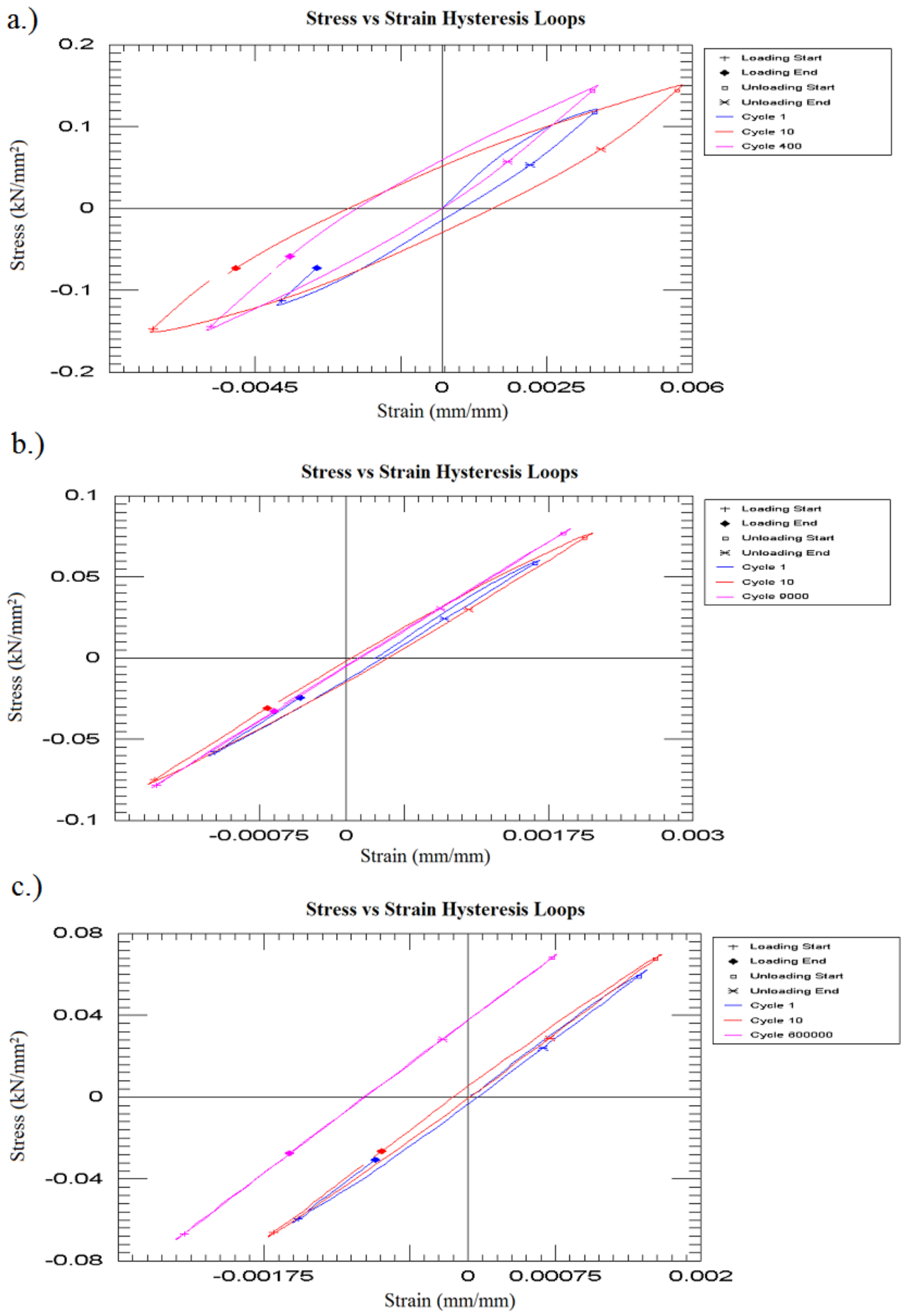

Figure 4.11: Hysteresis loops of the first cycle, tenth cycle, and mid-life cycle for, a.) 150 MPa stress amplitude, b.) 80 MPa stress amplitude, and c.) 70 MPa stress amplitude.

ing up to the mid-life cycle. An asymmetric tensile and compressive stress was observed in the hysteresis loops. From Fig. 4.12a.), during the first ten cycles while the machine was ramping up to the desired stress amplitude, the specimen underwent cyclic softening followed by cyclic hardening. After the tenth cycle, the plastic strain amplitude decreases almost linearly suggesting cyclic hardening occurred as the fatigue specimen was subjected to increased fatigue damage. The rate at which the plastic strain decreased in the high stress specimen was highest out of the three specimens.

For the 80 MPa specimen, the applied stress amplitude is below the experimental yield strength of the material. The first cycle hysteresis loop shows a smaller amount of plastic strain in comparison to the specimen tested at 150 MPa which is related to the difference in stress amplitude applied. The tenth cycle shows the largest plastic strain calculated in the specimen from the cycles plotted. At this cycle, the specimen experiences the desired stress amplitude for the first time. At the mid-life cycle, the hysteresis loop shows a more linear, almost elastic, loop. An asymmetric tensile and compressive behavior is still present in the data. During the first 10 cycles of the fatigue test, the specimen also undergoes cyclic hardening following by cyclic softening during the ramp up period to the desired stress amplitude, shown in Fig. 4.12b.). However, this behavior is not as pronounced in comparison to the higher stress specimen. After the tenth cycle, the calculated plastic strain decreases almost linearly until the end of the fatigue test, indicating cyclic hardening was occurring. The rate at which the plastic strain decreases is slower compared to the high stress specimen.

The fatigue specimen tested at 70 MPa represents the endurance limit of the material because it survived at least 10 million cycles and the specimen did not fail. The applied stress amplitude for this fatigue specimen is also below the experimental yield strength of the material. The first cycle in the hysteresis loop shows a small plastic strain is observed in the material. While this plastic strain is slightly increased at the tenth cycle because of the higher stress amplitude applied. At the mid-life cycle, the plastic strain is minuscule, and

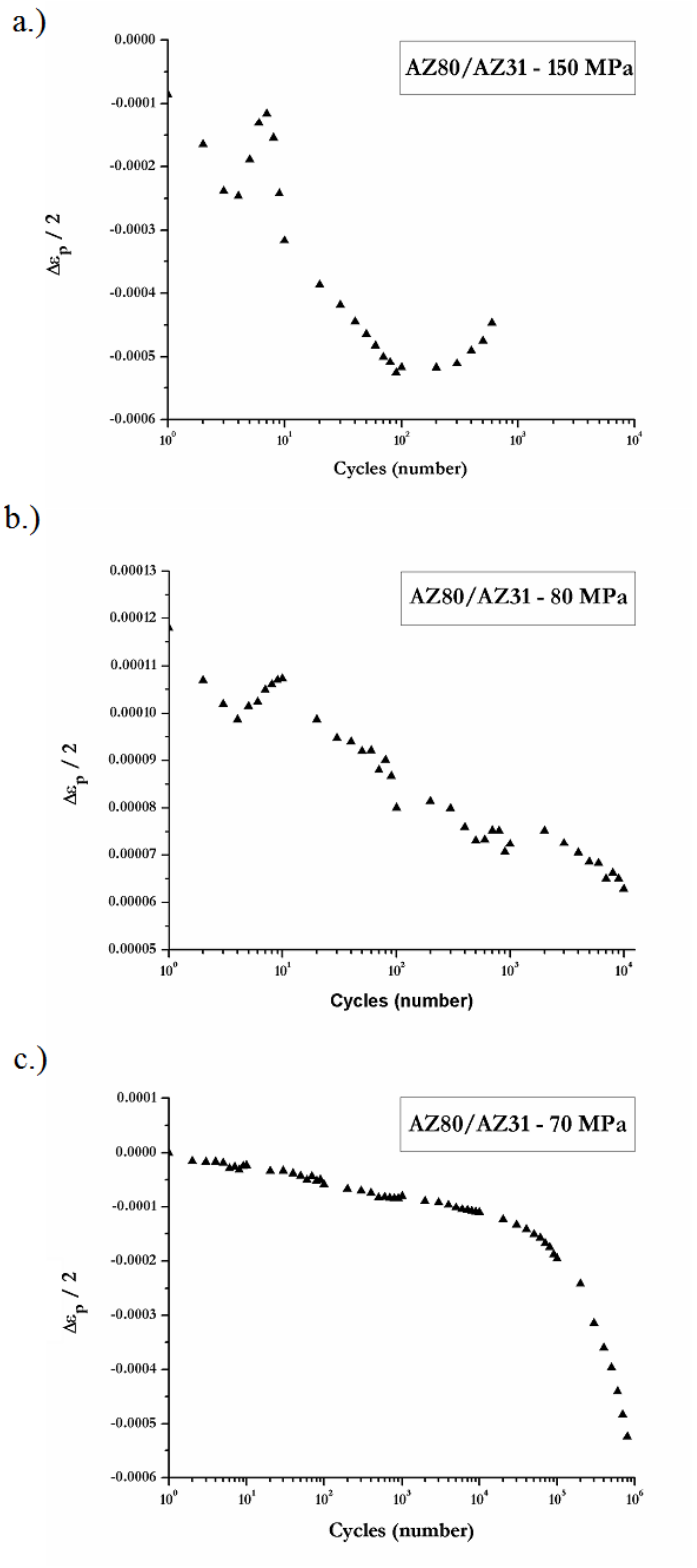

Figure 4.12: Calculated plastic strain vs. number of cycles to failure plot for, a.) 150 MPa stress amplitude, b.) 80 MPa stress amplitude, and c.) 70 MPa stress amplitude.

the hysteresis loop shows a pseudo-elastic behavior. An asymmetric behavior is again observed for the tensile and compressive stresses of the hysteresis loops. From Fig. 4.12c.), it is evident that the calculated plastic strain vs. cycles plot for the 70 MPa specimen is different than the specimens tested at the high and moderate stress amplitudes. Unlike the other specimens, during the first ten cycles where the fatigue test is ramping up to the desired stress amplitude the specimen did not experience a sequence of cycle hardening followed by cycle softening. Instead, the plot shows an almost linear decrease in plastic strain experienced by the specimen, indicating cycling hardening occurring. The decreasing rate of the plastic strain is much lower in comparison to the high and moderate stress amplitude. While the other specimens underwent a two-stage cyclic deformation process, the fatigue specimen tested at the endurance limit stress amplitude did not undergo the same process.

4.5 SEM Fracture Observations

The fracture surfaces of two specimens were analyzed by SEM microscopy to reveal the fracture mechanisms for the AZ80/AZ31 weld. The first specimen tested at the highest stress amplitude, 150 MPa, which had a fatigue life of 761 cycles, and the second specimen tested at a moderate stress amplitude, 80 MPa, which had a fatigue life of $18,815$ cycles. The latter specimen is located just before the sharp bend in the S-N curve for weld 32.

The observations of both specimens show evidence that crack nucleation occurred at the surface possibly due to a stress concentrator. Commonly, un-cracked specimens that undergo fatigue testing tend to have fracture initiating on the surface. Once initiated, the nucleated crack grew until the point where the remaining material was over stressed, which eventually leads to unstable crack growth and final fracture. The fracture surfaces of the specimens show macroscopic and microscopic features unique to fatigued materials.

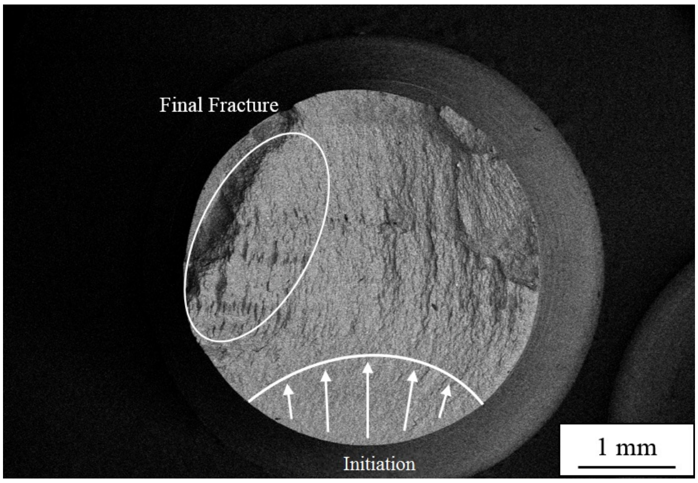

Figure 4.13: Low magnification image of fracture surface for the 150 MPa stress amplitude specimen.

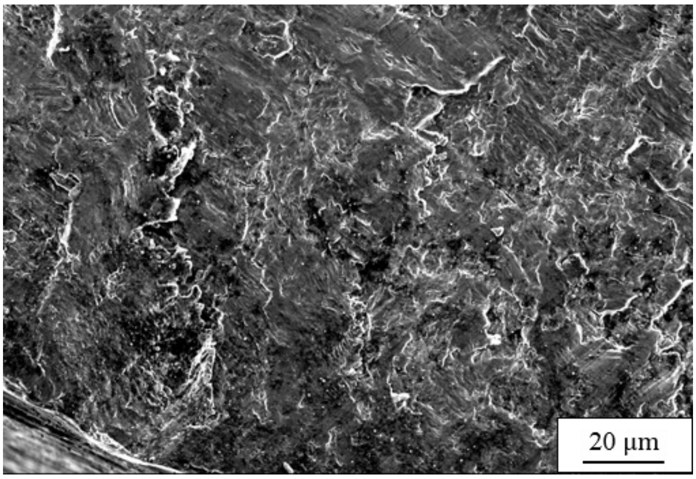

Figure 4.14: Surface texture near crack initiation for the 150 MPa stress amplitude specimen.

From Fig. 4.13, the crack initiation site, and final fracture region are identified. The fracture surface contains traces of both brittle and ductile fracture. At the initiation site, there is stable and rapid crack growth with minimal plastic deformation resulting in a smooth texture shown in Fig. 4.14. Both fractures surface for the high and moderate stress amplitude showed the evidence of beach marks imaged in Fig. 4.15 and Fig. 4.21, respectively. These beach marks, or clam shell marks, are produced by changes in the crack growth rates. They tend to indicate points during which the crack advance was altered during fatigue testing. The specimen tested at a higher stress amplitude had distinct fatigue striations shown in Fig. 4.16, while the specimen tested at the moderate stress amplitude it was not so apparent. In HCP materials, the formation of fatigue striations has been related to the twinning and detwinning during loading and unloading. The presence of striations is a unique feature to fatigue testing. During cyclic loading, once a crack is initiated, it begins to open as a result of the normal stresses applied and activates plastic slips at the crack tip. During loading the crack opens and the tip blunts, and during unloading the crack closes and the tip sharpens. After a complete cycle of loading and unloading, the crack grows a certain distance. This step-by-step process leaves behind footprints on the fracture surface referred to as striations. Striations are microscopic in nature and are visible under high magnification, however, beach marks are more macroscopic and can be seen with the naked eye. The fracture surface also shows cleavage steps and an indication of secondary cracks growing vertical to the crack growth direction present in Fig. 4.17. The final fracture region for the high stress amplitude is larger than that of the moderate stress which can be related to the difference in applied stress.

The fracture surface of the specimen tested at the moderate stress amplitude was noticeably different in comparison to the fracture surface of the higher stress amplitude. There were multiple crack initiation sites on the surface, with one main crack resulting in fracture,

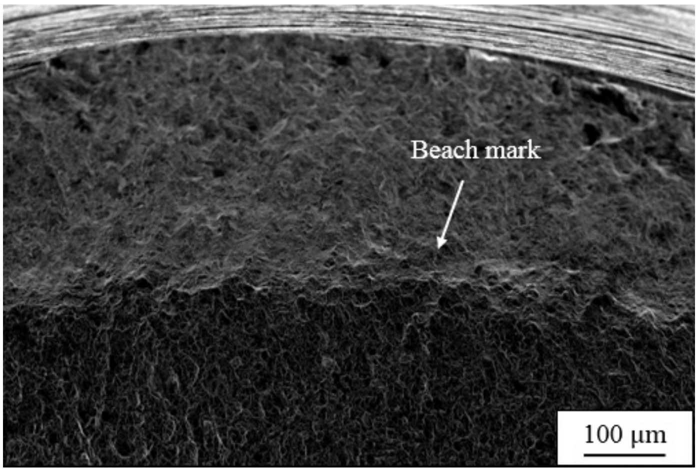

Figure 4.15: Beach mark on the fracture surface for the 150 MPa stress amplitude specimen.

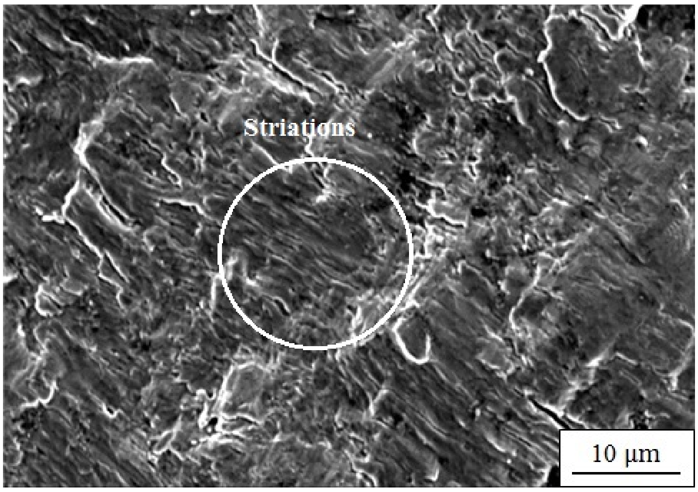

Figure 4.16: Fatigue striations on the fracture surface for the 150 MPa stress amplitude specimen.

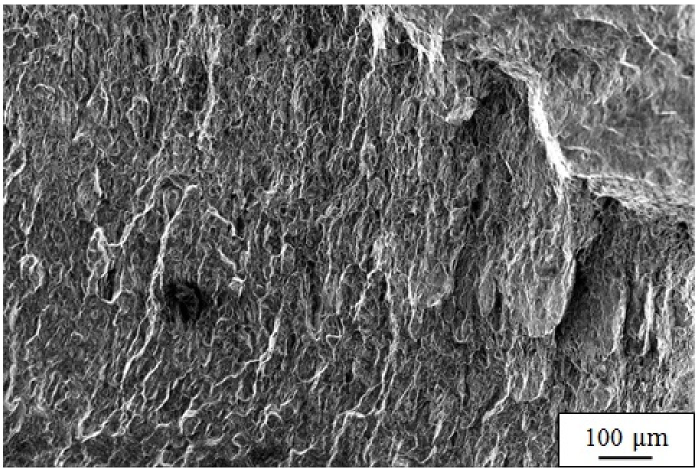

Figure 4.17: Angled cracking on the fracture surface for the 150 MPa stress amplitude specimen.

shown in Fig. 4.18. At the crack initiation site, it is evident there is a surface abnormality that likely became the primary stress concentrator. The surface texture near the main crack initiation site is shown in Fig. 4.20. The texture near the crack initiation site was very brittle, with almost no plastic deformation occurring indicating a crack had propagated through this region at a high rate. Cleavage edges were also evident pointing towards the direction of the specimen fracture.

The formation of ratchet marks was evident in the moderate stress amplitude fracture surface but not in the high stress amplitude fracture surface. Ratchet marks are macroscopic features on the fracture surface that are created when multiple cracks, initiated at different locations, join together creating steps on the fracture surface shown in Fig. 4.19. The small final fracture zone and the combination of these ratchet marks indicate that the stress applied was relatively light, but there were high stress concentrators leading to multiple crack initiation sites.

Similar to the higher stress specimen, the fracture surface for the moderate stress amplitude was neither true brittle nor true ductile. There were regions of brittle fracture that

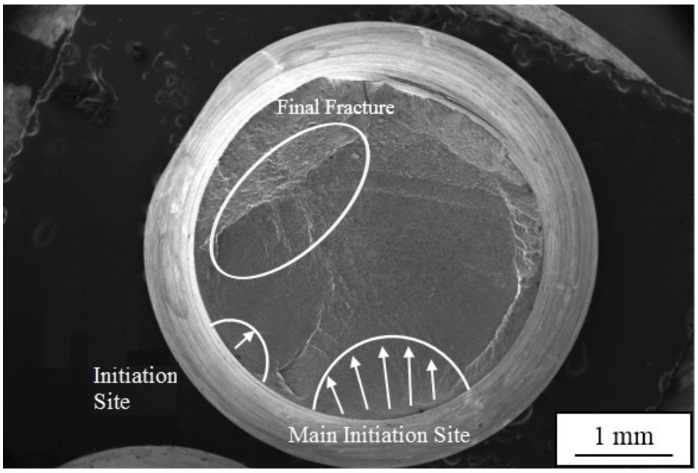

Figure 4.18: Low magnification image of fracture surface for the 80 MPa stress amplitude specimen.

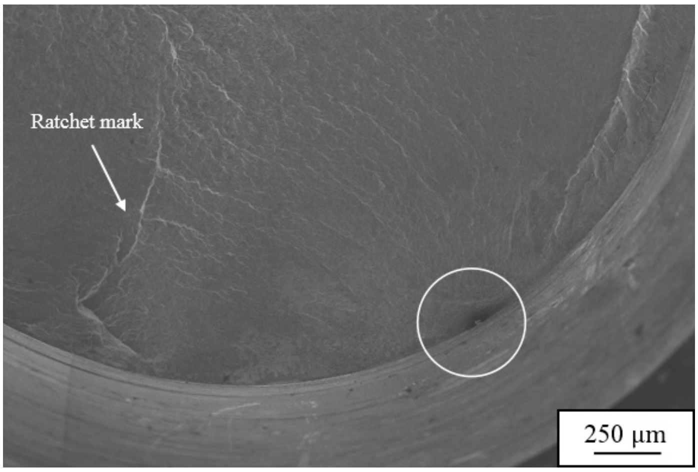

Figure 4.19: Main crack initiation site for the 80 MPa stress amplitude specimen.

transitioned to ductile regions interspersed with dimples and localized area of plastic deformation of the fracture surface shown in Fig. 4.22.

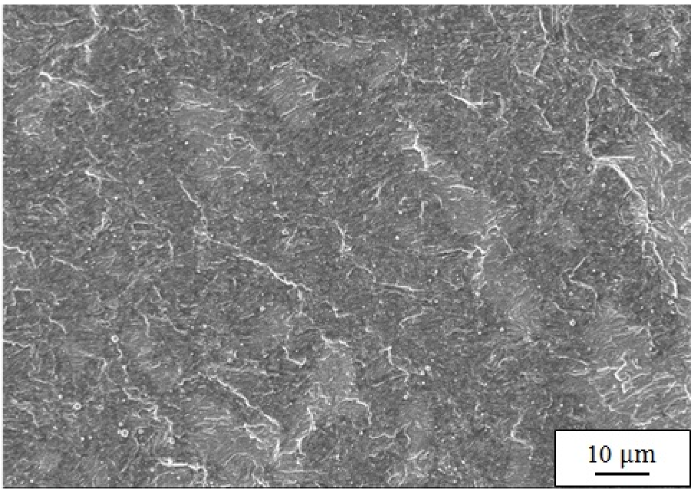

Figure 4.20: Surface texture near crack initiation for the 80 MPa stress amplitude specimen.

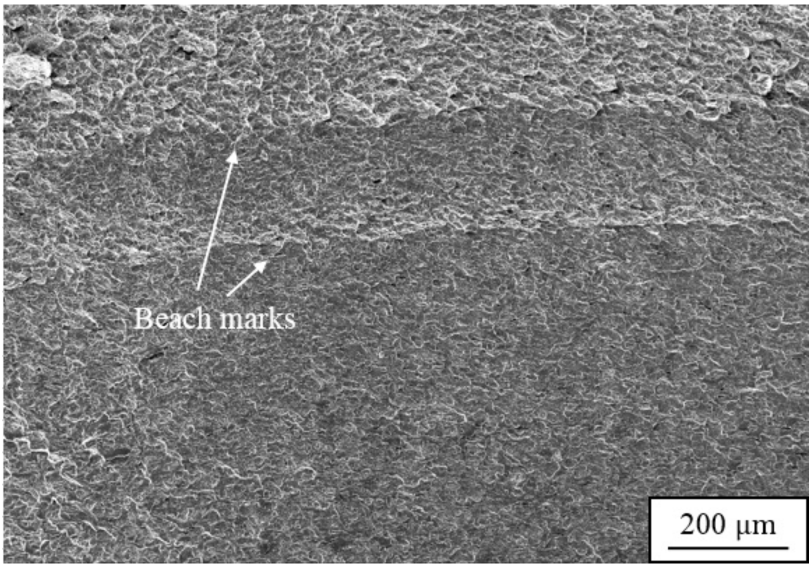

Figure 4.21: Beach marks on the fracture surface for the 80 MPa stress amplitude specimen.

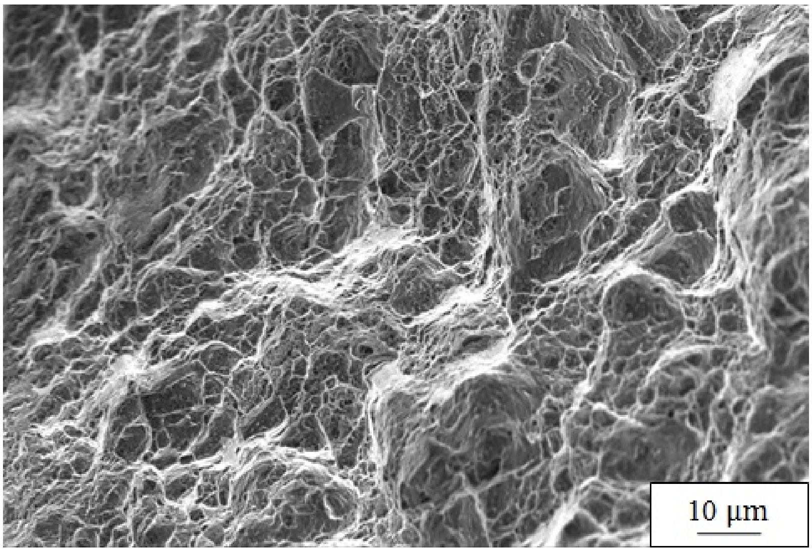

Figure 4.22: Angled cracking on the fracture surface for the 80 MPa stress amplitude.

4.6 TEM Observations

TEM studies of the microstructure were carried out on three selected fatigued specimens to identify the dislocation structure during various stages of fatigue and to determine characteristics of damage. The selected specimens are: i.) the highest testing stress amplitude of 150 MPa, with a fatigue life of 761 cycles, ii.) a moderate testing stress amplitude of 80 MPa, with a fatigue life of 18,815 cycles and just at the bend of the S-N curve, and iii.) the non-fractured specimen that represents the endurance limit of the material at a stress amplitude of 70 MPa.

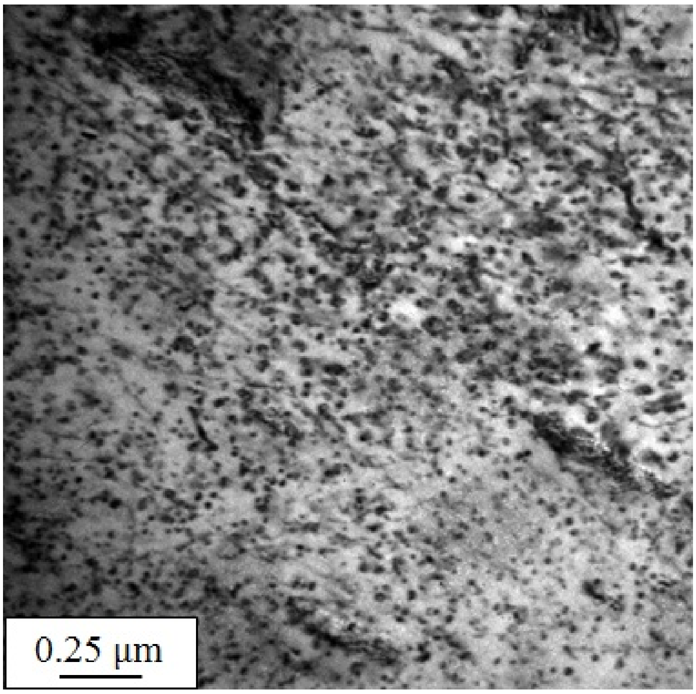

Figure 4.23: Bright field TEM image of the 150 MPa specimen showing densely packed dislocation loops and debris.

There were a large number of dislocation loops and dislocation debris located in the 150 MPa specimen, shown in Fig. 4.23. Out of all the specimens that were analyzed with TEM, the 150 MPa was the only one that showed evidence of a twin in the dislocation structure.

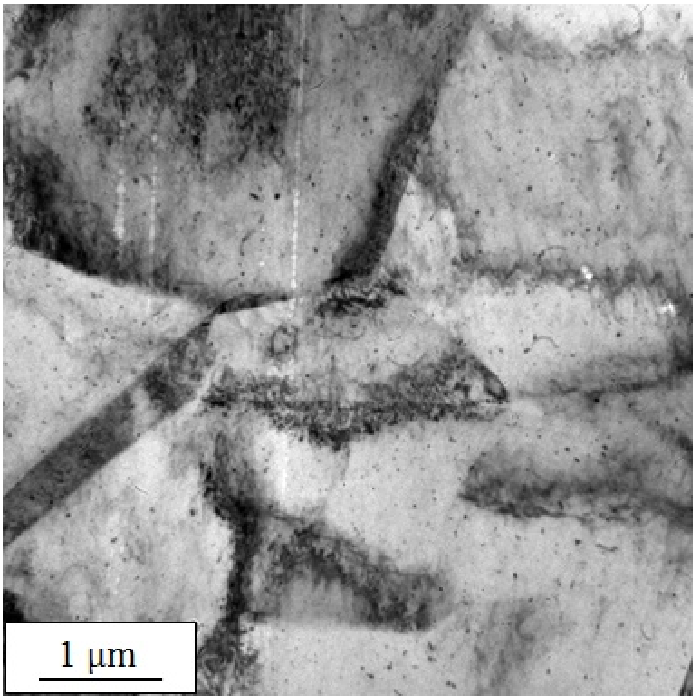

Figure 4.24: Bright field TEM image of the 150 MPa specimen showing a narrow twin, as well as multiple grains.

Fig. 4.24 shows the narrow twin that has a straight boundary with the matrix material. This twin could have formed as a result of the fatigue process, the material processing, or during the friction stir welding. It is likely that this twin formed as a result of the fatigue process because twins were not imaged in the other specimens. However, it is important to note that TEM analysis shows a localized region in the material.

Observation by dark field imaging techniques reveals the dislocation structure of this specimen, outlined in Fig. 4.25 and Fig. 4.26. There is a widespread distribution of linear and non-linear dislocation sections throughout the specimen. There is also evidence of dislocation dipoles in all the specimens imaged. These dipoles are unique features formed in the early stages of plastic deformation, where slip is constricted.

Also located in the 80 MPa specimen was a large quantity of dislocations and dislocation debris shown in Fig. 4.27. Similar to the 150 MPa specimen, there were dislocation

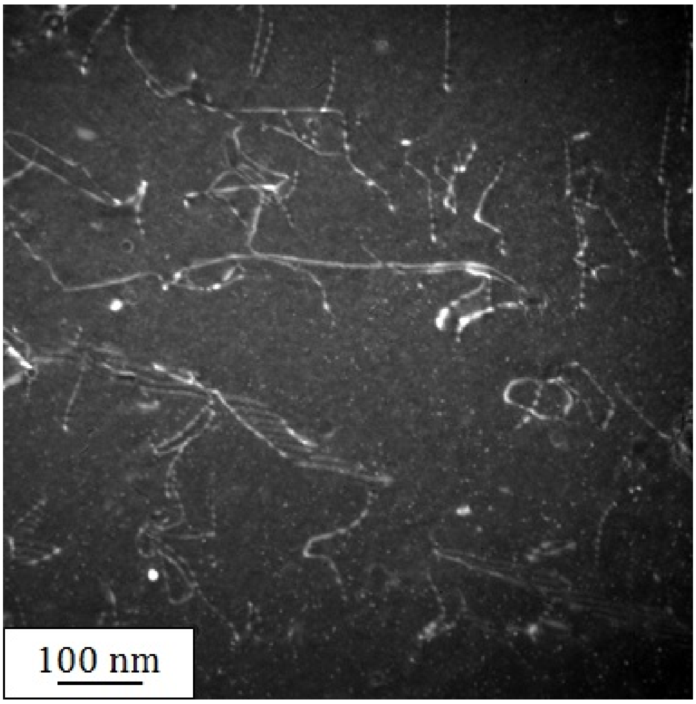

Figure 4.25: Dark field TEM image of the 150 MPa specimen showing stacking faults and dislocation network.

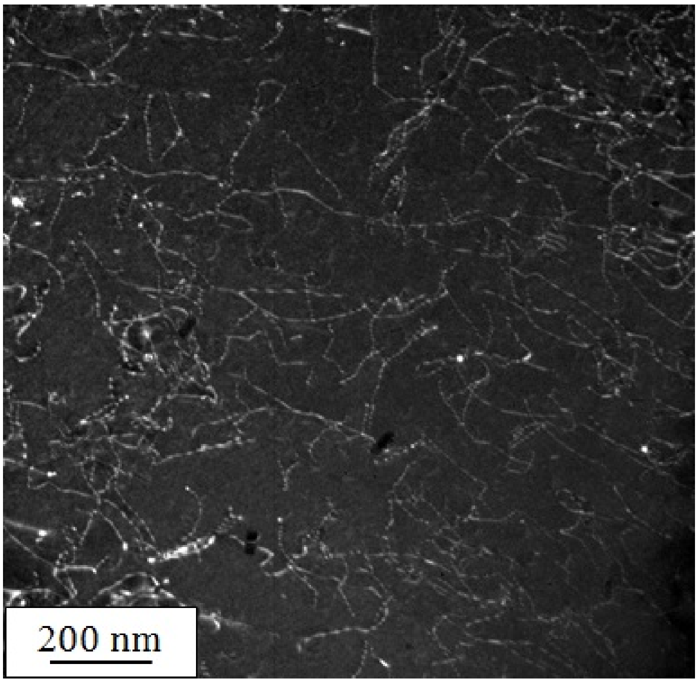

Figure 4.26: Dark field TEM image of the 150 MPa specimen showing dislocation network.

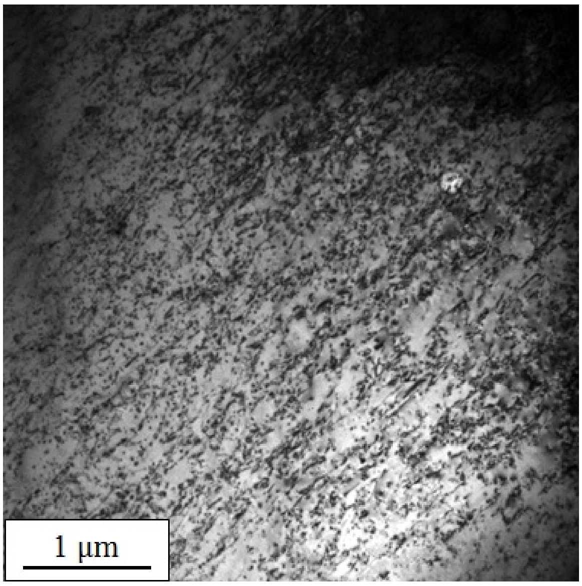

Figure 4.27: Bright field TEM of the 80 MPa specimen showing densely packed dislocation loops and debris.

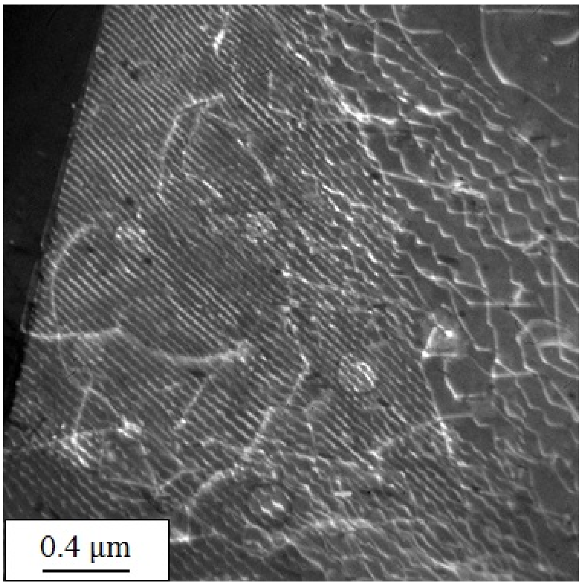

Figure 4.28: Dark field TEM image of the 80 MPa specimen showing dislocation network at the grain boundary.

dipoles present, as well as dislocation loops; however, there were no stacking faults imaged in this specimen. In comparison to the 150 MPa specimen, dark field imaging showed a less dense dislocation network which can be attributed to the difference in stress levels. The dislocation network is also made up of linear and non-linear dislocations shown in Fig. 4.28 and Fig. 4.29.

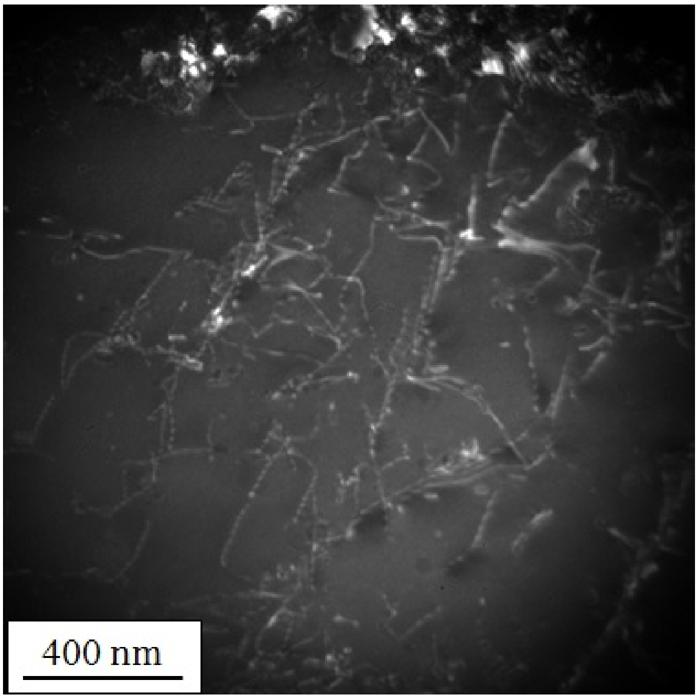

Figure 4.29: Dark field TEM image of the 80 MPa specimen showing dislocation network within a grain.

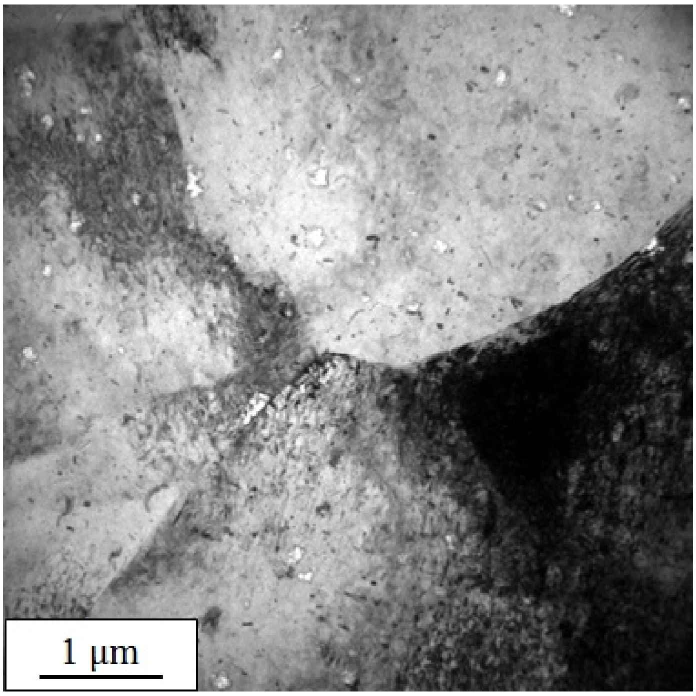

Figure 4.30: Bright field TEM of the 70 MPa specimen showing a triple grain boundary.

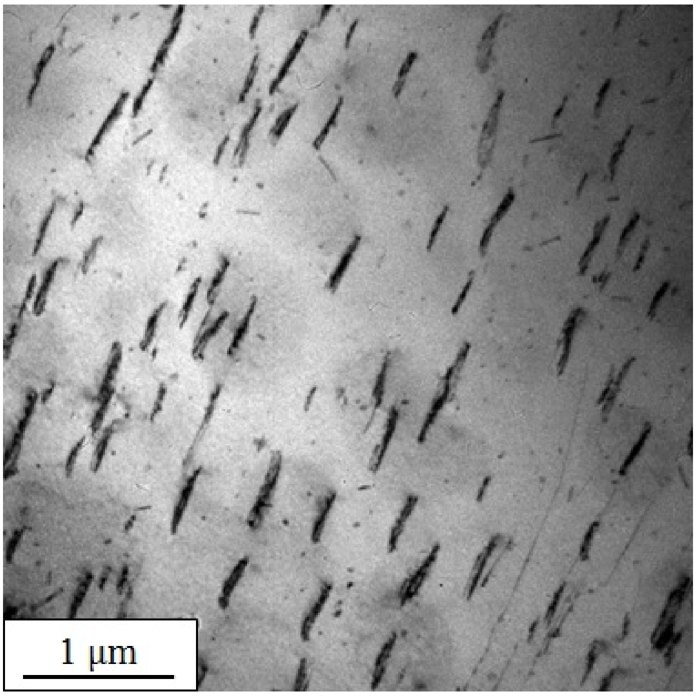

Figure 4.31: Bright field TEM image of the 70 MPa specimen showing dislocation loops close to the edge-on orientation.

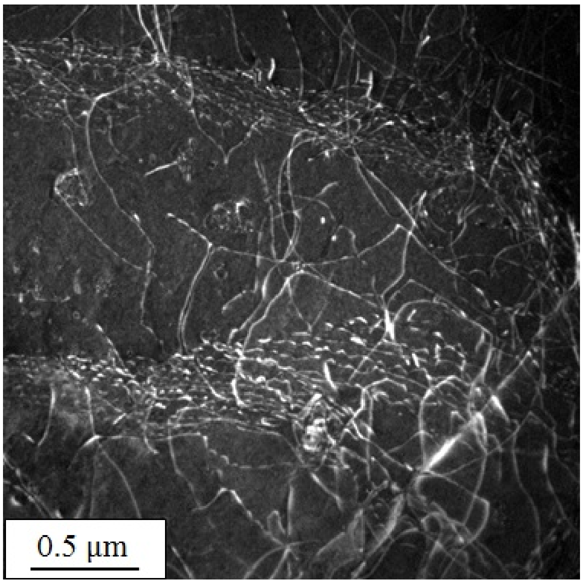

Figure 4.32: Dark field TEM image of the 70 MPa specimen showing dislocation network and dislocation pile up on grain boundary.

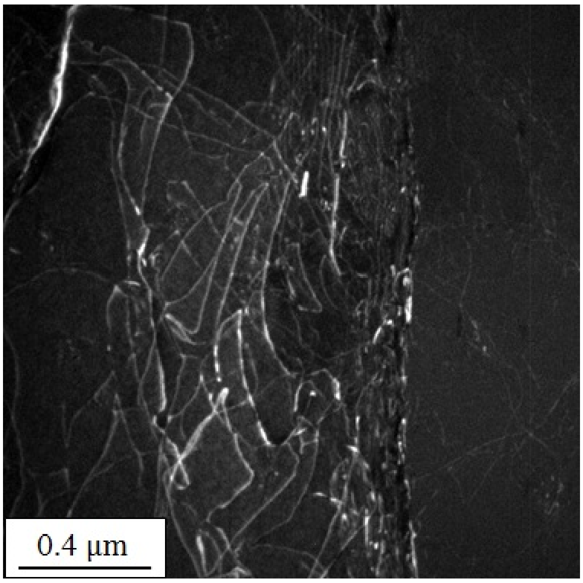

Figure 4.33: Dark field TEM image of the 70 MPa specimen showing dislocation network near the grain boundary.

The specimen tested at 70 MPa represents the endurance limit of the material because it did not undergo failure and had survived for over 10 million cycles. Thin foils were prepared from a similar location of the failure, with regards to previous specimens. Fig. 4.30 shows a triple grain boundary in the specimen with dislocations and debris piled up on the boundaries. There is evidence of dislocation loops and debris in the specimen, however, the density of the dislocation was much less in comparison to the high and moderate stress amplitudes. Although, the length of some of the dislocations was of the magnitude of approximately 0.5 μm. Similar to the past specimens, dark field imaging shows linear and a non-linear dislocation network present.

A unique observation in the 70 MPa specimen is the evidence of dislocations near grain boundaries as well as piled up dislocations that appear to form a sub-grain boundary, shown in Fig. 4.32 and Fig. 4.33. The dislocation pile-up on the grain boundaries may have hindered crack movement in the specimens. These boundaries can act as pinning points which impede further propagation of dislocations in the material. The dislocation network also shows the presence dislocation dipoles that was also observed in the other specimens.

4.7 Texture Measurements

Pole figures were obtained from fatigued specimens, as well as an undeformed specimen. The fatigued specimens that were used are 150 MPa, 80 MPa, and 70 MPa, representing the endurance limit. The data acquisition was done perpendicular to the loading axis. These specimens were also cut precisely in the same location; however, the nature of the welding procedure causes an asymmetry in the materials across the weld interface. The results from the raw data and incomplete pole figures are summarized in Fig. 4.34.

Initially, the (0002) pole figure for the undeformed specimen shows evidence of a strong

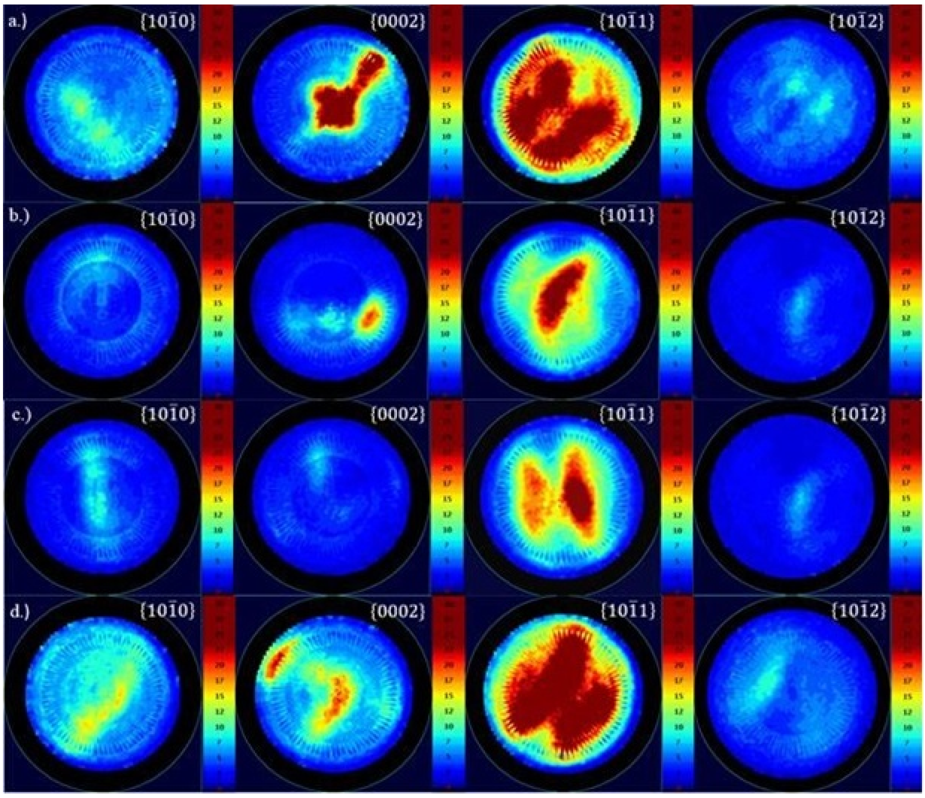

Figure 4.34: GADDS pole figures for: a.) undeformed specimen, b.) specimen deformed at 150 MPa, c.) specimen deformed at 80 MPa, and d.) specimen deformed at the endurance limit of 70 MPa.

basal texture developed during the extrusion process. However, as the specimens were cyclically deformed the strong basal texture becomes weaker and more washed out. The (0001) basal planes reorient approximately 60° off the tensile direction for the 150 MPa specimen. The pole figures for the 70 MPa specimen retain the some of the initial basal texture with a portion of the (0001) basal planes reorienting approximately 70° off the tensile direction. Nonetheless, qualitatively the 70 MPa specimen preserves the similar texture of the undeformed specimen even though it underwent significant fatigue damage. On the contrary, for the 80 MPa specimen, the basal texture becomes very weak, suggesting texture rotation during fatigue. The pole figure results do not show signs of mechanical twinning occurring in the specimen; this observation is consistent for all the specimens tested.

Calculated full pole figures were constructed for the present data using the GADDS incomplete pole figures as an input. Initially, the calculated pole figures were done using orthorhombic crystal symmetry; however, there was little correlation between the GADDS pole figures, as the material lacked some of the assumed symmetry MTex has used. Fig. 4.35 shows the calculated pole figures for the undeformed and fatigued specimens, 150 MPa, 80 MPa, and 70 MPa, respectively. The calculated pole figures shown assume a triclinic (no symmetry) crystal structure.

The pole figures obtained through MTex and GADDS correlate well with each other; however, in GADDS the pole figures obtained do not show data on the outer edges, at low angles of measurements. For the 80 and 70 MPa specimens, there is a strong basal texture shown on the MTex pole figures but not on the GADDS pole figures. The resulting calculated pole figures for these specimens show a basal texture occurring approximately parallel to the tensile axis. For these specimens, a portion of the basal texture rotates approximately 90° possibly due to the increased fatigue damage applied.

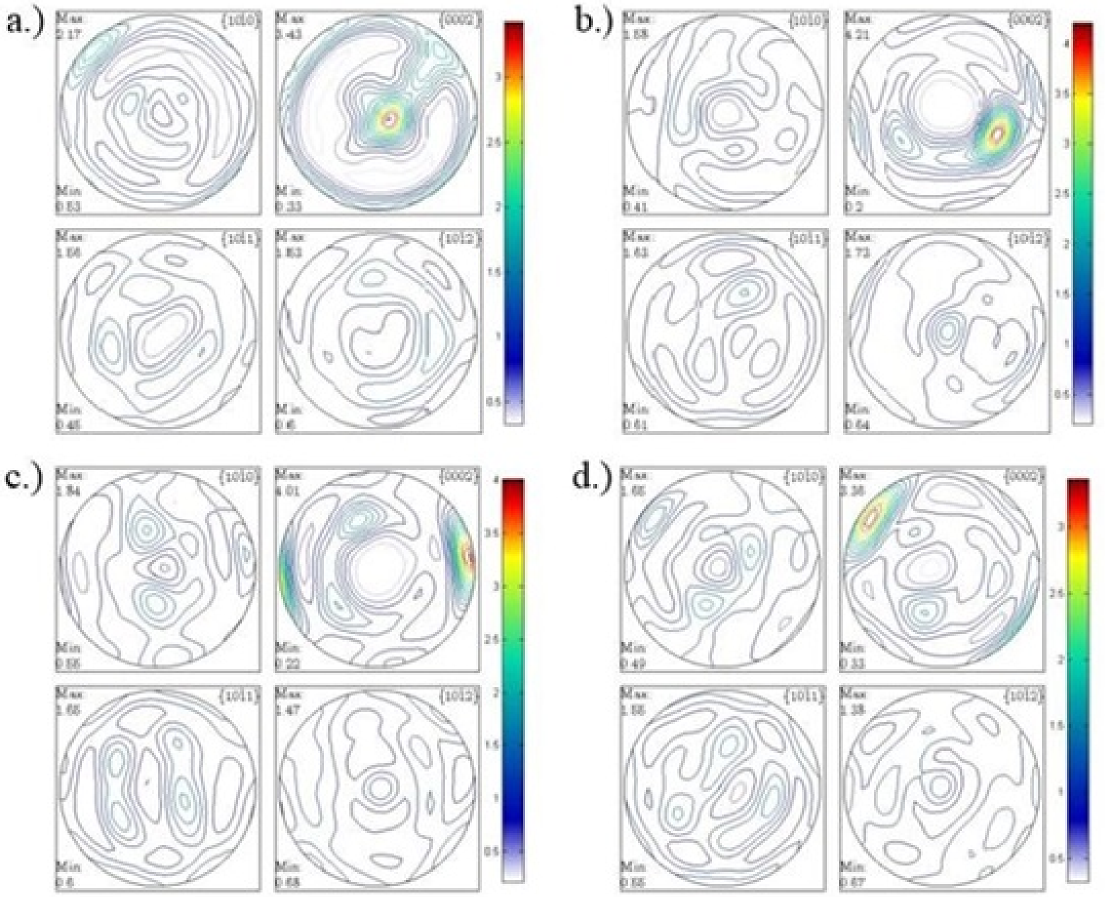

Figure 4.35: The calculated pole figures using MTex for: a) undeformed specimen, b) specimen deformed to 150 MPa, c) specimen deformed to 80 MPa, and d) specimen deformed to the endurance limit of 70 MPa.

Chapter 5

Discussion

Fully reversed, stress-controlled fatigue tests were conducted on dissimilar friction stir welded magnesium alloys. The fatigue behaviour of the welded alloys was investigated by plotting the applied tensile stress vs. the number of cycles until failure curve. Curves for the two dissimilar welds were constructed, with a more in-depth analysis completed for the AZ80/AZ31 weld.

In previous studies, the characterization of fatigue behaviour through S-N curves has been done for numerous magnesium alloys under varying manufacturing and surface preparation, as well as several different loading conditions. In the case of the magnesium alloys in the present study, several authors (Morita et al. [22], Tokaji et al. [23], Tsukikawa et al. [25], and Nan et al. [24]) had results that depicted a sharp bend in the S-N curve with a well-defined endurance limit. The results from these authors differed from each other, which solidifies the notion that the fatigue behaviour of materials is strongly influenced by the microstructure, surface preparation, as well as the loading conditions used. Nan et al. [24] carried out rotating bending fatigue tests on extruded magnesium AZ31, and it was found that the endurance limit of the material is 122.5 MPa. While Morita et. al [22] conducted axial load-controlled fatigue tests on extruded magnesium AZ31, and the results showed a sharp bend in the S-N curve with an endurance limit of 90 MPa. Only a few authors have investigated the fatigue behaviour of friction stir welded magnesium alloys in the present study. Tsujikawa and his colleagues [25] examined the fatigue strength of extruded similar friction stir welded magnesium alloys. Their results for the welded AZ31 show a well-defined endurance limit at 75 MPa, in comparison to the endurance limit of the base material which was 94.5 MPa; both materials had a sharp bend in the S-N curve. However, in the present work the fatigue behaviour of dissimilar magnesium alloys, AZ80/AZ31 and AZ80/AZ61, was investigated. The endurance limit of the AZ80/AZ31 weld was found to be 70 MPa for welds produced at 89 mm/min and 63 mm/min, with a sharp bend in the S-N curve. Although the endurance limit was not found for the AZ80/AZ61 weld produced at 89 mm/min, the S-N curve suggests a bend occurs around 90 MPa where the fitted curve begins to plateau. However, for the AZ80/AZ61 weld produced at 63 mm/min the endurance limit was found to be 90 MPa. Under stress-controlled testing conditions, the endurance limit of the material is primarily influenced by the strength of the material. The evidence of a sharp bend in the S-N curves of the present work coincides well with the previous authors that documented similar behaviour with the present materials used. Nan and his colleagues [24] found that in all their fatigued specimens, a crack initiated on the surface and propagated through the material. At a higher stress, this crack was able to propagate through the grains without being blocked, while at lower stress the crack growth was blocked. They suggested that the sharp bend in the S-N curve they obtained was due to a non-propagating crack being constrained by the phase change in the microstructure, resulting in crack arrest.

As it was previously mentioned, the S-N curve for the AZ80/AZ31 weld produced at 89 mm/min, showed specimens tested at 80 MPa and had fatigue lives of $18,815$ and $31,016$ cycles, while a decrease in stress amplitude of 10 MPa resulted in the fatigue life being

1.13×10^7 cycles. This results in the sharp bend shown in the present data which gives rise to the notion of an existing or lack of a non-propagating crack in the material during the fatigue process. The failure occurred for the specimens tested at 80 MPa and not at 70 MPa, which could be due to deformation mechanisms that are activated when a higher peak stress is applied. If there is an existence of a non-propagating crack at the endurance limit of the material, it is then likely that the crack ceases to grow as the critical stress intensity factor required to continue propagation is not achieved. On the other hand, a crack may also not continue to grow due to local inhomogeneities in the microstructure at the crack tip that impedes crack growth, acting as barriers. Alternatively, if a non-propagating crack is not present in the material at the endurance limit, then a microstructure or dislocation features that inhibit crack nucleation at a stress amplitude of 70 MPa is present. However, these features must not be able to impede crack nucleation at the higher stress amplitudes. There may be a series of micro cracks that have formed during the fatigue process, but the stress amplitude must not be high enough to cause the cracks to grow beyond a critical crack length. Since crack initiation period of a fatigue cycle may take up more than 90% of the total fatigue life of materials; a crack may form later in the fatigue process in the very high cycle fatigue region. The extent of the bend in the given S-N data can be further analyzed with extensive fatigue test around the endurance limit.

For the high stress, moderate stress, and endurance limit stress, the plastic strain vs. cycles plot showed cyclic hardening occurring at various rates after the desired stress amplitude was applied. The occurrence of cyclic hardening or softening is related to the dislocation microstructure of the material tested. The highly deformed material, thus having a high dislocation density, subjected to cyclic strains tend to have their unstable dislocation networks rearranged into more stable ones. This rearrangement reduces the stress required for plastic deformation to occur. Conversely, if the material has a low dislocation density and is subjected to cyclic strain, the deformation results in the introduction of new dislocations increasing the density. High strength metals tend to cyclically soften, while low strength metals tend to cyclically harden during fatigue. However, the behavior shown in the plastic strain vs. cycles plot for the endurance limit was different than what was observed in the high and moderate stress amplitude specimens. The sharp bend in the S-N curve occurs at the transition from the moderate to the endurance stress amplitude. The specimen tested at a moderate stress showed a sequence of cyclic hardening followed by cyclic softening in the ramping up period, but for the specimen tested at the endurance limit this behavior was not observed. The endurance limit specimen did not undergo a two-stage cyclic deformation process. Yet, the rate at which the plastic strain decreased during the fatigue process was the lowest in the endurance limit specimen. The plot showed an almost flat relationship which would have resembled a stable condition, where neither cyclic softening or cyclic hardening was occurring.

During mechanical testing, the total strain of a material consists of both an elastic and plastic component. The elastic strain component consists of strain that is reversible and material reverts to its original state after unloading. However, the plastic component results in the permanent deformation which is not recovered upon unloading. Although the stresses applied during the fatigue testing in the present work may lie below the experimental yield strength of the material, fatigue failure still occurred. The hysteresis loops of the fatigued specimens tested at a high, moderate, and endurance limit stress showed the presence of yield asymmetry. It has previously been found, a factor that results in this yield asymmetry comes from the presence of twinning and detwinning. During unloading, or in the present case reverse loading, twins in the material microstructure can disappear and consequently reappear under reloading. The stress ratio of the fatigue testing in the present work is equal to -1, indicating an equal tensile and compressive stress applied in one cycle. The yielding in the compressive state is a result of the activation of tension twinning as a deformation mechanism, which alters the c-axis orientation. Twinning plays a crucial role in the deformation of magnesium and magnesium alloys because it allows for the satisfaction of the von Mises$'$ criteria. Since magnesium has an HCP crystal structure, it has fewer slip systems than its counterpart metals that have a different crystal structure. Especially at room temperature where the CRSS of the predominate basal slip is low but lacks the desired five independent deformation systems for a homogenous strain to occur.

Furthermore, the stress analysis of the car rim was investigated by Ju [6], as well as Praveen and Gopichand [32]. The results that Ju obtained showed a peak stress of 21.45 MPa experienced at the joint of the hoop and spokes, while the stress in the other regions of the rim was around $14-18$ MPa. On the other hand, Praveen and Gopichand analyzed the stress for 4 different rim geometries and found a peak stress of $20-25$ MPa at the hoop of the rim. Both of these results are well below the endurance limit found for the AZ80/AZ31 weld, making it a viable option for use in service from a fatigue perspective.

To further investigate the fatigue characterization of the welds in the present study, an analysis of the failure locations with respect to the welds was carried out. Metallurgical welding has a randomness in comparison to mechanical joining because of the microstructure changes, surface defects, etc. that arise during the process. Friction stir welding produces an asymmetrical weld due to the tool rotation and the different heating effects that the advancing side and retreating side undergoes. The welding process yields four regions that are distinctively different in microstructure and properties; the weld nugget zone (WNZ), the thermo-mechanically affected zone (TMAZ), the heat affected zone (HAZ), and the base metal (BM). The regions are listed in order to proximity of the shoulder and pin. The WNZ region is comprised of small, uniform and equiaxed grains as a result of the pressure and rotation of the shoulder and pin, as well as the translation of the pin and shoulder.

The TMAZ region is located at the edge of the tool and experiences dynamic recovery and recrystallization at a high temperature due to the close proximity to the pin and shoulder. However, the HAZ region does not experience any mechanical deformation but instead goes through a heating process due to the heat conduction through the material. The temperature allows for dynamic recovery, but not recrystallization, resulting in much coarser grains. Like the name suggests, the BM region is not affected by the welding process, and the microstructure is similar to the starting material. Previous studies have shown that the HAZ has the lowest hardness values in comparison to the base metal because of the change in microstructure due to the thermal cycling.

Almost all the specimens in the present study, except those that fractured in the grips, had failed at the advancing side of the weld at the interface of the weld and base material of the AZ80. The schematic of the fatigue specimens with the respect to the weld was outlined earlier; it shows the nugget zone of the weld being centered at the transition from the grips to the gage length of the specimen. Whereas the interface between the weld and retreating side is located in the grips of the specimen. Although the grip does experience some fatigue damage, it is not exposed to the same extent of damage as the gage length. Initially, the two plates of AZ31 and AZ80 that were used for the friction stir weld were 5 mm thick, so the machined fatigue specimens obtained do not have any surface defects or any cooling rate differences from the bottom and top of the weld that arise from the welding process at the gage length. Microstructural analysis of the friction stir weld for the AZ80/AZ31 showed a change in the grain size between the weld and the AZ80 base metal in the gage length. Through the lineal intercept method, the average diameter of the grains is approximately 39.93 μm in the AZ80 base metal. While in the HAZ, the average diameter of the grains is approximately 20.34 μm. This change in grain size in the microstructure may result in a loss of ductility and have an increased local stress that differs from the rest of the gage length.

The fracture surfaces of fatigued specimens used for S-N testing were analyzed with the aid of a JEOL-6610LV scanning electron microscope. One fracture surface came from a high stress with a short fatigue life and the other from a moderate stress and a moderate fatigue life. The macroscopic features of the fracture surfaces are evidently different. It can be observed that for both amplitudes the specimens showed evidence of crack nucleation originating from the surface, which is observed in fatigue failure. Multiple initiation sites are observed in the moderate stress specimen, with the presence of ratchet marks, which indicate the boundary of two adjacent failure planes. Neither of the fracture surfaces was true brittle or true ductile fracture, instead, they were a mixture of both. The fracture surfaces show regions of stable crack growth where the crack extended through the material parallel to the loading axis. Along the fracture surfaces are beach marks which represent a substantial alteration in the component stress, and thus on the crack growth rate. Finally, the fast fracture region in both the fracture surfaces is comprised of various ductile voids and dimples, where the material is essential ripped apart. Additionally, through macroscopic examination, it can be estimated that there is a higher crack growth rate for the high stress specimen in comparison to the moderate stress specimen. Fatigue crack propagation was mainly characterized by fatigue striations along with secondary cracks, which were found to be perpendicular to the crack propagation direction. Fatigue striations were visible in the higher stressed specimen. However, they were difficult to detect in the moderate stress specimen. In previous studies, the presence of fatigue striations in magnesium alloys with a HCP structure is expected to be a result of twinning and detwinning in the compressive and tensile phase, respectively [21].

The fracture observations in the present work align well with the work of previous authors. Although the testing conditions and material are dissimilar, similar features unique to material fatigue was evident. The different features in the fracture surfaces led to the speculation that the sharp bend in the S-N curve is not a result of a rapidly propagating crack being block. Instead, the sharp bend could be a result of crack initiation occurring but without propagation due to the applied stress being below critical stress amplitude required for the crack to propagate and lead to fracture. If the latter is a result of the bend in the S-N curve, then it is anticipated that there will be a difference in the dislocation substructure for the specimens that failed and the one that did not fail at the endurance limit. Further analysis must be carried to characterize the fatigue behaviour of the material, particularly of the material substructure and dislocation features.

An observation of the dislocation substructure of three selected fatigued specimens was carried out using a Philips CM12 transmission electron microscope. The three fatigued specimens varying in stress amplitude applied, and fatigue life are; i.) the highest stress applied (150 MPa), ii.) a moderate stress (80 MPa) around the bend in the S-N curve, and iii.) a lower stress amplitude (70 MPa) representing the endurance limit of the material. Bright field TEM images show that the specimen at the highest stress contained the largest dislocation density, followed by the specimen tested at the moderate stress amplitude, and finally, the specimen at the endurance limit had the smallest dislocation density. The images of the dislocation density and debris observed in the three fatigued specimens showed an evolution of damage as a result of the fatigue testing. The 150 MPa specimen showed a very dense amount of dislocations in a small area, showing the extent of the damage applied. For the 80 MPa specimen, there is also evidence of a dense amount of dislocations but not as much as the 150 MPa specimen. However, for the 70 MPa specimen, the dislocation density is less in comparison to the previous specimens. But the dislocation loops observed are much larger, and some are even on the magnitude of 0.5 μm. Dislocation saturation may have occurred in this specimen, where there is an equilibrium between dislocations being produced and annihilation throughout the fatigue process. This specimen also had a very long fatigue life, without failure, which allowed dislocations to join but not grow past a certain critical length to initiate failure. The endurance limit specimen had evidence of dislocation pile-up that was imaged but was not seen in the other specimens. However, since TEM thin foils represent a small region in the specimen, dislocation pile-ups could have been present but not in the foils used for observation. An explanation for the S-N curve could be the presence of grain boundary strengthening occurring in the endurance limit specimen and not present in the other specimens tested at different stresses. Dislocations pile up on slip planes at grain boundaries, and these boundaries act as pinning points which impede further propagation of the dislocations in the material.

In previous work, Stevenson and Vander Sande [18] characterized the cyclic deformation of magnesium single crystals under strain-controlled loading conditions. They found that at low plastic strain amplitudes, the deformation mechanism for single crystals is essentially single slip. While at higher plastic strain amplitudes, the occurrence of duplex slip was observed in the material. In the specimens observed, it is probable that a stress dependant dislocation process occurs at higher stress amplitudes resulting in irreversible plastic deformation that inevitably leads to failure. Failure occurring in the high and moderate stress specimens but not in the lower stress specimen could be a result of the higher stresses causing other slip planes to become active, which has a compounding effect, triggering interactions with other various slip systems. Which governs the speculation that crack propagation is impeded below a certain critical stress amplitude. Another explanation for the dislocation behaviour in the present work can be the effect of the applied reaching a critical value that results in the generation of Frank-Read loop dislocation sources. Under this applied stress, dislocations are generated from existing dislocations in the material, either as a result of material processing or the friction stir welding.

The thin-foils used for TEM observation represent a localized region of the specimen. Thus many more thin-foils must be analyzed to have a thorough analysis and fully characterize the deformation structure and mechanism present in the material. At that point, it can be determined if the development of these dislocations during fatigue have an influence on the bend in the S-N curve. Also, an analysis of the dislocation substructure of the as-received specimens before fatigue would be imperative to grasp an idea of the bigger picture.

Texture analysis was performed on selected fatigued specimens, as well as an undeformed specimen, by X-ray diffraction (XRD). The fatigued specimens that were used are the ones tested at 150 MPa, 80 MPa, and 70 MPa. Initially, the undeformed specimen showed two preferred orientations of the grains with the $\{0002\}$ and $\{10\bar{1}1\}$ texture as a result of the extrusion and welding process in the incomplete pole figures. The 150 MPa specimen showed a more refined basal pole figure such that the $\{0002\}$ direction is roughly 60° off the tensile direction. The basal texture for the 80 MPa becomes very weak and almost non-existent. For the specimen tested at the endurance limit, a weaker basal texture reappears, with a portion of the grains orientated approximately 70° off the tensile direction. The extent of the weld asymmetry can be seen in the variation of the texture in the pole figures shown. Calculated pole figures used MTex show the texture of the specimens at higher angles that were outside the scope of the GADDS program, thus not seen in the incomplete pole figures. The calculated pole figures show that for the 80 MPa and 70 MPa specimens, a majority of the grains in the $\{0002\}$ pole figure rotated parallel to the basal plane.

In previous studies, Yu et al. [37] showed that twinning in magnesium can result in a drastic change in texture. They found that extension twinning along the $\{10\bar{1}2\}$ plane reorients the basal pole around 86.3°. This drastic change in the rotation of the basal texture seen in the 80 and 70 MPa specimens may be a result of the welding process, the fatigue process, or a combination of the both. The textures seen in the 80 and 70 MPa specimens have similar features, yet they differ in fatigue life significantly. To recall, the specimen tested at a stress amplitude of 80 MPa had a fatigue life of $18,815$ cycles, while the specimen tests at a stress amplitude of 70 MPa had a fatigue life in excess of 1.13×10^7 cycles. Keeping this in mind, along with the texture similarities of the two specimens, a variation of 10 MPa in the stress amplitude results in a 600 times increase in fatigue life which could be a result of a stress dependent dislocation process evident in the 80 MPa specimen but not in the 70 MPa specimen.

In the present study, the fatigue behaviour of friction stir welded magnesium alloys was characterized through the aid of mechanical testing, scanning electron microscope fracture surface analysis, transmission electron microscope dislocation substructure investigation, and X-ray diffraction texture analysis. The fatigue life of a material is generally characterized by the number of stress or strain cycles required for the material to fail. However, this number is a function of many variables, such as the stress level, loading conditions, fatigue environment, surface conditions and microstructure of the material. Previous studies have stated that the fatigue behaviour of materials is largely influence by their microstructures. Thus, small changes in the materials microstructure, surface conditions, and loading conditions may result in very different fatigue behaviour results. The S-N curves in the present study show an endurance limit of 70 MPa for the AZ80/AZ31 friction stir weld produced at welding speeds of 89 mm/min and 63 mm/min. For the AZ80/AZ61 weld produced at 89 mm/min, there is a plateau in the S-N curve around 95 MPa, but none of the samples tested lasted for the minimum requirement to be classified as the endurance limit of the material. A more detailed S-N curve for this weld can be completed with further fatigue testing. While for the AZ80/AZ61 weld produced at 63 mm/min, the endurance limit was found to be 90 MPa. It is worth mentioning that the endurance limit of a material is not an absolutely or fully repeatable number, for reasons stated previously. Several identical specimens cut from the same locations may produce different endurance limit values when tested, however, may still falling within a range that can be found through a statistical analysis. Nevertheless, the value obtained for the endurance limit for the AZ80/AZ31 weld is greater than the stresses found by Ju et al. in their stress analysis of a rim.

At room temperature, the primary deformation systems for hexagonal close-packed structures, such as the magnesium alloys used in the present study, are $\{0002\}$ basal slip and $\{10\bar{1}2\}$ twinning due to their low critical resolved shear stress values. In the present study, XRD analysis shows a strong preference for basal grain orientation. This grain orientation rotates approximately 90° for the 80 and 70 MPa specimens which could be as a result of twinning activity in the material that causes a drastic change in texture. During testing, the tensile stress applied the $\{10\bar{1}2\}$ twinning may cause an extension along the c-axis of the crystal structure. The lack of preference for basal orientated grains in the texture data leads to the speculation that the stresses applied resulted in other slip systems to be activated. The texture data also shows an increase in grain orientation of the prismatic plane when there is a rotation of the basal plane in the specimens. However, there may be deformation mechanism that is stress dependent because failure occurred in the 80 MPa specimen, but not for the 70 MPa specimen. The evidence of ratchet marks on the fracture surface for the 80 MPa sample also shows that multiple cracks initiated and grew, but their propagation was impeded to a certain extent by the material. Previous studies have shown that the texture varies along the friction stir weld. FSW is a mechanical welding technique which results in a weld asymmetry along the materials, which results in an even more variation in texture across the weld interface. If the orientation of neighbouring regions in the material is different, stress may localize here, and the region may accommodate or be resistant to slip.

The results depicted in the present study show a preliminary investigation of the fatigue behaviour of friction stir weld of AZ80/AZ31. However, the orientation of the weld and the fatigue specimen have a heavier emphasis on the interface between the weld and advancing side of the material, which in this case is AZ80. Further fatigue testing is required to produce S-N curves for specimens that contain both interfaces of the weld with the base materials. Inherently, the S-N curves for these specimens will be different than the ones in the present work because they will contain differing microstructures.

Chapter 6

Conclusions

Stress controlled fatigue testing of dissimilar magnesium friction stir welded alloys was carried out. The fatigue behaviour was characterized and the material substructure was investigated. The most important conclusions arising from this work are as follows:

1. There is a sharp bend in the S-N curves with a well-defined endurance limit at 70 MPa for the AZ80/AZ31 welds produced at welding speeds of 89 mm/min and 63 mm/min. There was no endurance limit found for the AZ80/AZ61 weld produced at a welding speed of 89 mm/min, however, the endurance limit of the weld produced at 63 mm/min was found to be 90 MPa. Therefore, present results suggest therefore are enhanced fatigue properties for the AZ80/AZ61 welds over AZ80/AZ31 welds produced at the same welding speeds of 89 mm/min and 63 mm/min. The S-N curves for the combined fatigue data of the different welds showed reproducible results in the fatigue testing.

2. SEM fracture surface analysis shows crack initiation occurring on the surface for both the 150 MPa and 80 MPa specimens. Neither fracture was true brittle or true ductile, while both fracture surfaces showed evidence of beach marks which are an indication of a change in crack growth during fatigue. Ratchet marks were observed on the 80 MPa specimen, resembling multiple crack initiation sites.

3. The selected fatigued specimens for TEM analysis showed an evolution of fatigue damage in dislocation development which is related to the varying stress amplitude applied, as well as fatigue lives of the specimens. The dislocation density was the largest in the 150 MPa specimen and smallest in the endurance limit specimen at 70 MPa, which did not fail. Also, TEM microscopy of the 150 MPa showed a narrow twin in the dislocation substructure, while it was not imaged in the other samples. In addition, dislocation pile-up was imaged in the 70 MPa which may be an artifact of a crack being impeded in the material substructure.

4. Microstructure analysis of the AZ80/AZ31 weld showed a changed in the grain size during the transition from the weld to the AZ80 base metal. The average diameter of the grains is approximately 39.93 μm in the AZ80 base metal. While for the heat-affected zone, the average diameter of the grains is approximately 20.34 μm.

5. Texture analysis shows a strong initial basal texture in the undeformed material, attributed to the material processing and friction stir welding. The texture of the 150 MPa specimen showed that the basal texture was rotated roughly 60° off the tensile axis. However, for the 80 and 70 MPa specimens, there was an approximate rotation of 90°of the basal plane. The endurance limit specimen, 70 MPa, retained some of the initial texture, with a portion being rotated off the basal plane. This basal plane rotation can be a result of twinning occurring in the material from the fully-reversed stress profile carried out during the fatigue testing.

The global vision of this project was to improve the fuel efficiency of a vehicle by ultimately reducing its weight. More specifically, the development of an optimized low weight spare wheel, composed of AZ80 alloy for the hoop and the AZ31 or AZ61 alloys for the spokes. To further implement magnesium and its alloys into modern day vehicles, welding procedures and the integrity of the welds must be analyzed thoroughly. The present work analyzed the fatigue behavior of the friction stir weld of AZ80 and AZ31. The S-N curve observed shows an endurance limit of 70 MPa. From previous work, finite element analysis has shown the peak stress in a car rim has been roughly 25 MPa, thus leading to the conclusion that the present material can meet the fatigue requirements in place. However, further study needs to be carried out to characterize the material dislocation substructure to verify if it attributes to the bend observed in the S-N curve. Also, further fatigue testing of the different sections of the weld is required to analyze the effect of the changing microstructure on both the advancing and retreating side of the friction stir weld.

It is also important to mention that further research is required to characterize the corrosion behavior and resistance of the material, as well as material processing in large scale production. If this friction stir weld magnesium alloy prototype wheel is to be implemented, it will result in a reduction in the vehicle weight. Although there may not be huge changes in fuel efficiency from reducing the curb weight alone, it does have a compounding effect. Wheel weight is a key component in the un-sprung mass of a vehicle; a lighter wheel will be easier to spin and stop which is crucial for city-driving. One of the biggest challenges for auto makers is to design a vehicle that is fast and powerful, yet comfortable and safe – while still being affordable. There is no single solution to reach the requirements set out by Corporate Average Fuel Economy (CAFE) for 2025. Light weighting a vehicle is a compounding effect, with a lighter vehicle you will required a smaller engine, thus a smaller transmission, and so on. These changes to the vehicles, no matter how small, will add up to have a significant effect on the overall efficiency.

Bibliography

[1] Astm standards - standard practice for codification of unallyed magnesium and magnesium-alloys, cast and wrought.

[2] M.H. Yoo. Slip, twinning, and fracture in hexagonal close-packed metals. *Metallurgical Transactions*, 1991.

[3] Z.Y. Ma R.S. Mishra. Friction stir welding and processing. *Materials Science and Engineering Reports*, 2005.

[4] Fumiaki Hiura. Latent hardening in pure magnesium single crystal. Master's thesis, McMaster University, 2008.

[5] C Laird. The influence of metallurgical structures on the mechanism of fatigue crack propagation. *TRANS METALL SOC AIME*, 1966.

[6] B.J. Diak O. Ojo W.D MacDonald M. Niewczas F. Ju, Z. Xia. Magnesium technologies sp-2205. In *SAe International*, 2008.

[7] Zygo.

[8] ASM International. Chapter 14 - fatigue. *Elements of Metallurgy and Engineering Alloys*, 2008.

[9] J. Lindemann P. Zhang. Influence of shot peening on high cycle fatigue properties of the high-strength wrought magnesium alloy az80. *Scripta Mater. 52*, 2005.

[10] J. Polmear. Magnesium alloys and applications. *Materials Science and Technology*, 1994.

[11] Michael M Avedesian, Hugh Baker, et al. *Magnesium & Magnesium Alloys*, chapter Grades and Alloys. ASM International, 1999.

[12] D.J. Bacon D. Hull. *Introduction to Dislocations*. Elsevier, 2011.

[13] Standard terminology relating to fatigue and fracture testing - e1823 96.

[14] H.E. Boyer. *Atlas of Fatigue Curvers*, chapter Fatigue Testing, page 10. American Society of Materials, 1986.

[15] E.N. Diaconescu G. Frunza. Hysteresis and mechanical fatigue. *The Annals of University "Dunarea de Jos" of Galati*, 2006.

[16] A. Halfpenny. A practical discussion on fatigue. *Managing Durability*, 2008.

[17] L. Anquez P. Rabbe. *Fatigue of Materials and Structure Fundamentals*, chapter Fatigue Crack Initation, page 43. ISTE Ltd., 2010.

[18] J.B. Vander Sande R. Stevenson. The cyclic deformation of magnesium single crystals. *ACTA Metallurgica Vol. 22*, 1974.

[19] Y. Jiang Q. Yu, J. Zhang. Fatigue damage development inpure polycrystalline magnesium under cyclic tension-compression loading. *Elsevier*, 2011.

[20] V. Skorik J. Muller L. Wagner F. Novy, M. Janecek. Very high cycle fatigue behavior of as-extruded az31, az80, and zk60 magnesium alloys. *International Journal of Materials Research*, 2009.

[21] X.M. Yang S.D. Wu S.X. Li G.Y. Li S.M Yin, F. Yang. The role of twinning-detwinning on fatigue fracture morphology of mg-3*Elsevier*, 2008.

[22] N. Ohno Y. Kawakami T. Enjoji S. Morita, S. Tanaka. Cyclic deformation and fatigue crack behavior of extruded az31b magnesium alloy. *Materials Science Forum*, 2010.

[23] Y. Ishiizumi N. Hasegawa K. Tokaji, M. Kamakura. Fatigue behavior and fracture mechanism of a rolled az31 magnesium alloy. *International Journal of Fatigue*, 2004.

[24] T. Goshima R. Nakanishi Z. Nan, S. Ishihara. On the sharp bend in the s-n curve of the az31 extruded magnesium alloy. *Scripta Materialia*, 2007.

[25] K. Higashi H. Iwasaki T. Hasegawa A. Mizuta M. Tsujikawa, H. Somekawa. Fatigue of welded magnesium alloy joints. *Material Transactions*, 2004.

[26] F. Renner H. Zenner. Cyclic material behavior of magnesium die castings and extrusions. *International Journal of Fatigue*, 2002.

[27] M. Tsujikawa M. Hins T. Hirata K. Higashi T. Morishige, A. Kawaguchi. Dissimilar welding of al and mg alloys by fsw. *Materials Interaction*, 2005.

[28] K. Nakata D. Liu, H. NIshio. Anisotropic property of material arrangement in friction stir welding of dissimilar mg alloys. *Materials & Design*, 2011.

[29] D. Wang B.L. Xiao Z.Y. Ma J. Yang, D.R. Ni. Strain-controlled low-cycle fatigue behavior of friction stir-welded az31 magnesium alloy. *The Minerals, Metals, & Materials Society and ASM International*, 2013.

[30] S.D. Bhole X. Cao S.M. Chowdhury, D.L. Chen. Effect of pin tool thread orentation on fatigue strength of friction stir welded az31b-h24 mg butt joints. *Procedia Engineering*, 2010.

[31] V. Balasubramanian G. Padmanaban. An experimental investigation on friction-stir welding of az31b mg alloy. *International Journal of Advanced Manufacturing Technology*, 2010.

[32] D. Gopichand P. Praveen. Geometrical optimization and evaluation of alloy wheels four wheeler. *International Journal of Research and Innovation*, 2014.

[33] R. Rotinat F. Pierron J.-E. Masse L. Commin, M. Dumont and L. Barrallier. Influence of the microstructural changes and induced residual stresses on tensile properties of wrought magnesium alloy friction stir weld. *Material Science and Engineering*, 2012.

[34] Y. Xiao Z. Zhou D. Liu, R. Xin and Q. Liu. Strain localization in friction stir welded magnesium alloy during tension and compression deformation. *Material Science and Engineering*, 2014.

[35] A.P. Gerlich M.R. Daymond J. Hiscocks, B.J. Diak. Influence of magnesium az80 friction stir weld texture on tensile strain localization. *Material Science and Technology*, 2016.

[36] E112- 12 standard test methods for determining average grain size.

[37] Z.Feng Z. Yu, H. Choo and S.C. Vogel. Influence of thermo-mechanical parameters on texture and tensile behavior of fricton stir processed mg alloy. *EScripta Materialia*, 2010.